

**Collision cross sections for identical and non-identical rare-gas  
atom pairs for energies from 0.01 eV to 10 keV.**

**ONLY FIGURES (NOT FIGURE TITLES OR TEXT) ARE  
VALID BEYOND SECTION IV. EVERYTHING IS SUBJECT  
TO CHANGE**

A. V. Phelps

*JILA, University of Colorado and National Institute of  
Standards and Technology, Boulder, Colorado 80309-0440*

(Dated: December 5, 2004)

**Abstract**

Differential and angular integrated cross sections for elastic collisions of identical rare gas atoms He-He, Ne-Ne, Ar-Ar, Kr-Kr, and Xe-Xe are recommended for collision energies from  $\sim 0.01$  eV to 10 keV. Cross sections are also presented for He-Ar, Ne-Ar, and Ne-Xe. The data includes calculations of elastic scattering that utilize potential energy curves for large internuclear separations previously determined from near thermal transport, virial coefficient, and scattering data. At small separations we use published theoretical calculations for the lighter identical atoms and their extrapolation to pairs involving Xe. The scattering phaseshifts are calculated using the JWBK approximation as described previously for Ar-Ar. The calculated cross sections are compared with published scattering experiments and transport coefficient analyses. Extrapolations of experimental elastic and inelastic differential cross sections are used to estimate the reduction in the integral cross sections caused by inelastic collisions for He-He, Ne-Ne, Ar-Ar, and He-Ne. Total and viscosity cross sections are fitted with empirical functions for energies from  $\sim 0.01$  eV to 10 keV to facilitate their use in plasma models. Published comparisons of experimental and theoretical integral inelastic cross sections are reviewed and corrected where necessary.

PACS numbers: PACS numbers: 34.50.-s; 34.20.-b; 52.20.Hv

## I. INTRODUCTION

Integrated and differential cross sections for use in modelling discharge plasmas, shock waves, etc. in rare gases are recommended for energies from 0.1 eV to 10 keV. Because of our interest in transport phenomena, such as the flow of energy to electrodes via fast atoms, we emphasize the large angle scattering that dominates, for example, the viscosity cross section. Our starting point for each atom-atom pair is a calculation of cross sections for elastic scattering. We compare these results with experiment over a wide energy range and consider the modifications of the cross sections resulting from inelastic scattering at the higher energies. We provide approximate analytic expressions to our recommendations for use in plasma models. In some cases, this includes the highly anisotropic differential scattering cross sections that are found over the whole energy range of interest. I NEED TO DO THIS FOR He AND Ne.

Experiments [1–3] and models have shown the importance of fast atoms with energies from 10 to 1000 eV in plasma-surface interactions [1, 4–11] and in the production of excited and ionized atoms in plasmas [1, 3–5, 9, 11, 12]. Recent applications for rare-gas atom pairs include: Hartmann et al [13], He-He; Oh et al [14], Xe-Xe; Bogaerts [15], Ar-Ar; Donkó [16], Ar-Ar; Revel et al [17], Ar-Ar; Hagelaar et al [18], Ar-Ar; Capedeville et al [19], Ar-Ar and Ne-Xe; Bánó et al [20], He-Ar; The calculation of elastic scattering cross sections for H atoms with various atoms, e.g., H, D, T, and He, has received considerable attention recently in connection with modelling of edge effects in fusion devices [21–23]. Also, models [24] of shock waves have made use of energy dependent atom-atom scattering cross sections from thermal energies up to roughly 1 eV. In some these cases the cross sections used differ from the results presented here by more than an order of magnitude. Of course, the importance of such errors depends on the individual problem.

The analysis of viscosity, thermal conductivity, and isotopic diffusion coefficient data to determine effective cross sections and interaction potentials for symmetric and asymmetric rare-gas atom pairs at energies below roughly 1 eV is discussed in many textbooks [25–27] and review papers [28, 29]. Over 30 years ago, experimental measurements of scattering of He by He[30–33] and other gases and of theoretical investigations[34–37] provided a good understanding of the principals involved in the elastic, inelastic, and ionization collisions of rare gas atoms. More recently, empirical total scattering and ionization[38] cross sections

have been reviewed. The theoretical and experimental data for Ar-Ar atom scattering has been reviewed and the elastic scattering theory extended to higher energies[11]. Unfortunately, there does not seem to be a modern review of the available data for other rare gas atom pairs or of inelastic data.

In Sec. II We begin with a brief discussion the definitions of the cross sections of interest in this review. Our interaction potentials and theoretical elastic differential cross sections integral cross sections are presented and compared with available experiments in Sections III through X. In these sections we review the limited data on the effects of inelastic collisions on the cross sections and estimate the effects of inelastic collisions on integrated transport cross sections for some of the gas pairs. In Appendix A and B we present analytical fits to the theoretical results. We do not discuss data for collision energies below 0.01 eV or above 10 keV.

## II. CROSS SECTION THEORY SUMMARY

This section is a condensed review of the definitions of the cross sections used in this paper. See Ref. [11] for a more complete summary of the theory of our calculation of elastic scattering as applied to Ar-Ar. Expressions for the observables of interest in terms of these scattering phaseshifts are somewhat different depending on whether the two atoms are identical or nonidentical particles. Reference [27] gives the formulas only for the nonidentical case, which is relevant to He-Ar. formulas for the identical atom case are discussed by ???????. For non-identical atom case, the differential scattering cross section is

$$I(\theta, E) = |f(\theta, E)|^2, \quad (1)$$

where the scattering amplitude is given by

$$f(\theta, E) = \frac{1}{2ik} \sum_{l=0}^{\infty} (2l+1) \left( e^{2i\delta_l(E)} - 1 \right) P_l(\cos \theta). \quad (2)$$

Three observables of interest for transport problems and beam experiments are obtained from integrals over the elastic differential scattering cross section. The first of these is what we will call the beam attenuation cross section defined by

$$\sigma_{att} = 2\pi \int_{\theta_d}^{\theta_{max}} I(\theta) \sin \theta d\theta, \quad (3)$$

Here  $\theta_{max} = \pi$  for asymmetric collisions and  $\theta_{max} = \pi/2$  for symmetric collisions. In beam attenuation experiments the lower limit  $\theta_d$  is set by the angular aperture of the atom detector [39, 40]. We follow the convention of calling the cross section obtained when  $\theta_d \rightarrow 0$  the total cross section  $\sigma_t$  [25–27, 41]. As we will see in section III B, experimental values of  $\sigma_{att}$  are generally much smaller than  $\sigma_t$ , so that  $\sigma_t$  becomes an idealized quantity of principal interest as a means of comparing theories or as a numerical reference in modelling. Note that what we call the total cross section has been termed the elastic cross section in several recent papers [22, 23]. We avoid this terminology because the viscosity and diffusion (where applicable) cross sections are also elastic in the conventional sense that the processes they describe do not lead to a change of the internal energy of the colliding atoms.

Equation 3 can also be used to calculate integrated or total inelastic cross sections. Here a small value for the lower limit  $\theta_d$  is less critical because the inelastic scattering occurs at relatively large angles. See, for example, section III C. A problem to be cited later is that there are different conventions as to the upper limit  $\theta_{max}$  to be used in the case of symmetric collisions. Theoreticians conventionally use  $\theta_{max} = \pi/2$  in order to avoid counting "events" twice, whereas experimentalist conventionally normalize their results to the collection of all of the photons or ion-electron pairs produced and so use  $\theta_{max} = \pi$ .

The integral viscosity cross section appears in transport models when one is concerned with the angular distribution of the scattered atom, rather than just that scattering took place. It is the simplest precisely-defined measure of the importance of large angle scattering in symmetric atom-atom collisions. It is particularly important in plasma modelling because it is a measure of the resistance of the gas to energy transport, e.g., to first order the viscosity cross section determines the thermal conductivity of a gas [25–27]. The viscosity cross section [25–27, 41] for the symmetric case is

$$\sigma_v = 2\pi \int_0^{\pi/2} I(\theta) \sin^3 \theta d\theta. \quad (4)$$

For the asymmetric case the integral extends from 0 to  $\pi$ .

The third transport cross section of interest here is that for diffusion [25–27, 41], used to describe the random walk motion of one type of atom through a gas of other atoms. This

cross section is often called the momentum transfer cross section, although it equals the diffusion cross section only for elastic collisions [41]. This cross section only has meaning for distinguishable particles as for the asymmetric or heteronuclear scattering case and is given by

$$\sigma_d = 2\pi \int_0^\pi I(\theta)(1 - \cos \theta) \sin \theta d\theta, \quad (5)$$

### III. HE-HE RESULTS

#### A. He-He interaction potentials

Figure 1 shows interaction potentials versus internuclear separation for two He atoms from various sources. Here the radius is on a logarithmic scale to emphasize the smaller radii. Also, the larger values of the potential are plotted on a logarithmic scale while the lower values are plotted on a linear scale. Potentials predicted by theory and derived from beam scattering experiments are shown by the points. Recent theory and experiment for the larger separations has been reviewed and correlated by Aziz and collaborators [42, 43] and leads to the dashed curve (which coincides with the solid curve at large radius). At intermediate radius we show results from experiment [44, 45] and theory [46–48]. Our calculation using Gaussian98 [49] are shown by the solid points. At large separations this theory gave poor results and is not shown. The dotted line at very small radii shows the Coulomb interaction potential for two helium nuclei. The points shown by crosses near 0.1 bohr are derived from the measured [50] scattering of  $\text{He}^+$  by He. As for  $\text{Ar}^+$  scattering by Ar, this curve is very close to the theoretical results for neutral atoms[11].

The solid curve shows our adopted ground state interaction potential. This potential uses an analytical fit to a modified screened Coulomb formula [51] for small radii and a formula from Ref. [42] at larger radii. We did not utilize the most recent results [43] because of their analytical complexity and the small change in the potential caused by “retardation” effects. A number of authors [30, 31, 34, 37, 52] have discussed the potentials for excited states of  $\text{He}_2$  (not shown). In general, it is found that the excited states and the ground state approach closely and or cross at radii of  $\sim 1.2$  bohr and less. Their effects on differential cross section are cited in Sec. III C. The analytic formula for our adopted ground state

potential is given in Appendix A.

## B. He-He attenuation cross sections

In this section we are concerned with the beam attenuation cross section or just the attenuation cross section defined by Eq. 3. It is obtained experimentally by measuring the exponential attenuation of a narrow beam of He atoms under conditions in which multiple collisions with He atoms can be neglected. It varies with the angular size of the atom detectors. Theoretically, it is calculated by applying Eq. 3 to the differential cross sections or its equivalent in terms of scattering phase shifts [11]. In the limit of a very small detector one obtains the sum of the elastic and inelastic angular-integrated cross sections that is independent of detector size. We will call this limit the total cross section. Although the cross sections obtained using the larger detector areas are sometimes also called total cross sections, we recommend against this terminology because of the dependence of this cross section on the apparatus dimensions. In theory papers [23, 53] and at energies below excitation threshold the is is often called the integrated elastic cross section or simply the elastic cross section. Because of the vagueness of the abbreviated terminology elastic cross section, we recommend against using it.

Figure 2 shows beam attenuation cross sections  $\sigma_{att}$  as a function of the angular half-width subtended by the He atom detector. The smooth curve shown is obtained by applying Eq. 3 to the elastic differential cross sections calculated using our adopted potential. The angle independent scattering at small angles and the structure near  $0.1^\circ$  are caused by quantum mechanical diffraction effects [27]. The experimental points shown for angles greater than  $0.1^\circ$  are taken from the measurements and compilation of Newman *et al* [54]. The older data was obtained [45, 54–58] in the course of determinations of the intermediate radius interaction potentials. The points shown at  $0.018^\circ$  are obtained by extrapolating the differential cross sections of [54, 59] to zero and integrating from 0 to  $90^\circ$ . These experimental results agree very well with the theoretical  $\sigma_t$  values cited in Sec. III E. In addition, the agreement of the calculated and measured  $\sigma_{att}$  values constitute a successful test of our theoretical model for the smaller scattering angles. The relatively recent results of Ruzic and Cohen [60] for 200 and 750 eV lie significantly above and below, respectively, those of Fig. 2. Note that the effects of inelastic collisions at large angles shown in Fig. 3 are just becoming noticeable at

the largest angles shown in Fig. 2.

The use of measured  $\sigma_{att}$  values in isotropic scattering models instead of  $\sigma_v$  has greatly overestimated the large angle scattering that is important for limiting fast-atom transport in moderate and high pressure plasmas. See, for example, the use of the results of Ref. [44] in Ref. [13].

### C. He-He differential cross sections

Differential cross sections for He atom-He atom collisions expressed in the "reduced" form [61] of  $\rho(\tau) = \theta * \text{Sin}(\theta) * I(\theta, E)$  versus  $\tau = \theta * E$  are shown in Fig. 3. Note that the  $\rho(\tau)$  functions are not symmetric about  $\tau/E = 90$  deg, as are  $I(\theta)$  values. The results of our JWKB calculations using the interaction potentials are shown by the solid curve of figure 1 for a relative energy of 750 eV. The symmetry oscillations have been removed by averaging the calculation over an angular range comparable with the experimental angular resolution. The points show the experimental sum for all scattering processes measured by Newman *et al* [54] and by Nitz *et al* [59] for the same relative energy. In this figure, the experimental  $I(\theta, E)$  in the laboratory frame have been converted into center-of-mass values [62]. The relative  $\rho$  values of Brenot *et al* [32] for the dominant elastic and inelastic processes are renormalized, i.e., increased by  $\approx 3$ , to our theory at their smallest angles, where elastic scattering is dominant. We have shown data for their nearest relative energy of 1000 eV. Figure 3 also compares our theoretical elastic scattering results with measured  $I(\theta, E)$  for excitation and ionization [30–32, 34] for their relative collision energy  $E$  of 1000 eV.

The departure of the sum of the differential scattering cross sections from the elastic scattering results beginning at  $\tau \approx 3$  keV-deg is attributed to the effects of inelastic scattering. The decrease in the experimental elastic differential cross section is particularly rapid and is similar to that observed for strong absorption cases in nuclear collisions [63]. The energy-loss experiments [31, 32] show that the excitation predominantly results in the excitation of either one or two atoms to the first group of excited states. Theory and experiment [32] show that principally  $2^1P$  states are excited. The sum of the differential cross sections for ionization is also shown. The collision products change from an ion plus atom to an ion plus an excited atom as the collision energy increases [32]. CHECK THIS From figure 3, we see that inelastic collisions resulting in small angle scattering is very unlikely. Because

of symmetry, this data also implies small scattering near 180 deg. This means that inelastic scattering for classically low impact parameter trajectories and close distances of approach is very small and elastic scattering probably occurs. This reasoning is consistent with Brenot *et al* [32] statement that elastic scattering rises toward the calculated elastic scattering curve at large angles.

Olson *et al* [34] and Gauyacq [35, 37] calculate differential cross sections for excitation of He( $2^1P$ ) and He( $2^1S$ ) in He-He collisions for collision energies from 50 to 250 eV. They obtain rather good agreement with the relative experimental results of Morgenstern *et al* [31] for energies of 100 to 200 eV. Integrated cross sections are discussed in Secs. III D and III E.

#### D. He-He integrated inelastic cross sections

Figure 4 shows excitation and ionization cross sections for symmetric He atom-He atom collisions. The curves show the results of photon and electron collection experiments integrated over the usual  $180^\circ$  in center-of-mass. The points show the results of theoretical calculations and scattering experiments, but integrated over  $180^\circ$ , instead of the  $90^\circ$  conventionally used for identical atom scattering theory and scattering experiment[64].

At low energies the dominant process is the excitation of the  $2^1P$  state resulting in the excitation of one or both atoms[31, 32] and the emission of 58.4 nm radiation[33, 65, 66]. At higher energies excitation of other states of He is observed from emission [65], but is difficult to detect from scattering measurements. Ionization cross sections are determined by the collection of electrons[67] and by collecting scattered and energy analyzed ions[30]. Other ionization data is compared the values shown here in Ref. [38]. The crosses in figure 4 show upper limits to the sum of the inelastic cross sections as calculated using the cut-off angles discussed in section III C and assuming that the sum of the differential cross sections is equal to the values obtained in our JWKB calculation of elastic scattering. Because the data of Fig. 3, and similar data for other rare gas pairs, show that the sum of the differential cross sections in the angular range of strong inelastic effects is roughly half the calculated elastic scattering, we expect the crosses to be roughly twice the actual sum of the inelastic cross sections[68]. This ratio is consistent with the experimental data of figure 4 and sets upper limits to the metastable excitation discussed below.

We show the calculated He( $2^1P$ ) excitation cross sections of Olson et al. [34] and of Gauyacq [35, 37] in Fig. 4. For collision energies above roughly 100 eV, the theoretical integrated excitation and ionization cross sections are remarkably close to experiment without making the adjustment in experimental magnitude previously proposed [35, 37]. It would appear that the theory misses a  $2^1P$  excitation channel near threshold.

After the application of the factor of two for different angular integration ranges, the agreement between theory [35, 37] and experiment [67] is as good as one can expect. The spectra of electrons ejected in ionizing He-He collisions has been measured and used to test models of the collisions [69].

Direct excitation of the He( $2^3S$ ) metastable state in He-He collisions appears to occur only when two-electron excitation of the He-He molecule occurs, followed by dissociation in which both atoms are excited [32, 35] or when one atom is ionized and one is excited [32]. According to Gauyacq [35], excitation of electrons in each atom to the 2s orbital is comparable with single excitation of the 2p orbital and subsequent  $2^1P$  production from threshold to 100 eV, but is smaller at higher energies. However, the fraction leading to direct excitation of  $2^3S$  is apparently unknown. Excitation of  $2^3S$  via cascading from higher levels is roughly an order of magnitude smaller than  $2^1P$  excitation [70]. The data for 587.6 radiation from the  $3^3D$  state and subsequent He( $2^3S$ ) production appears to be inconsistent between Ref. [65] and Ref. [70]. We have chosen the energy dependence of the former and the magnitude of the latter reference. Theory [35] suggests that excitation of the higher states shown occurs via the two-electron excitation process. As a tentative sum of excitation cross sections for the He( $2^3S$ ) metastable state in He-He collisions we suggest 20% of the theoretical  $2^1P$  excitation cross section. IS THE USE OF THE CONVENTIONAL "TWO-ELECTRON EXCITATION" TERMINOLOGY CLEAR ENOUGH? I LIKE "TWO-ATOM EXCITATION" BECAUSE THAT IS WHAT THE EXPERIMENT SEES, BUT THEORETICIANS LIKE TWO-ELECTRON EXCITATION OF THE TEMPORARY MOLECULE.

Direct excitation of the He( $2^1S$ ) metastable states in He-He collisions can occur via excitation of the 1s orbital [34, 35, 37] or when two-electron excitation of the He-He molecule occurs [35, 37]. Including both processes leads to a somewhat larger  $2^1S$  cross section [35]. The He( $2^1S$ ) metastable is also produced by cascade excitation from the  $2^1P$  state, but imprisonment of the 58.4 nm resonance radiation is required for efficient metastable production [71]. Additional  $2^1S$  production occurs through cascading from the  $3^1D$  state of

Fig. 4. As a tentative sum of excitation cross sections for the He( $2^1S$ ) metastable state in He-He collisions and in the absence of imprisonment of the 58.4 nm radiation, we again suggest 20% of the theoretical  $2^1P$  excitation cross section.

### E. He-He transport cross sections

Figure 5 shows total  $\sigma_t$  and viscosity  $\sigma_v$  cross sections versus center-of-mass energy for symmetric He-He collisions. The  $\sigma_t$  is appropriate to models of beam experiments, while the  $\sigma_v$  is more useful in models of swarm and discharge experiments. The uppermost set of curves and points show the total cross section  $\sigma_t$  as defined in Sec II. The solid curves are the results of our elastic scattering theory using the potential shown by the solid curve of figure 1. The double-dot-dashed line shows that  $\sigma_t$  values calculated using only the long-range, van der Waals interaction [51] and the small angle scattering model of Massey and Mohr [72] are within a factor of three of the detailed theory and experiment. The  $\sigma_t$  points at energies below about 0.1 eV are representative of measurements[73] showing oscillatory structure at very low He-He collision energies. The  $\sigma_t$  points at above 250 eV are "total" cross sections obtained by combining differential cross section measurements at low [54] and high [59] angular resolution, extrapolating to zero and  $90^\circ$ , and applying 3 from zero to  $90^\circ$ . We note that in spite of the inelastic effects discussed in Sec. III C there is good agreement between the sum of the elastic and inelastic cross section measurements and elastic scattering theory for energies below 3000 eV. This presumably reflects the fact that the total cross section is more heavily weighted toward smaller scattering angles and larger radii of closest approach, where in elastic effects are relatively unimportant.

The lower solid curve in figure 5 is the results of our calculation of the elastic viscosity cross section  $\sigma_v$  using the adopted potential of figure 1. The crosses show  $\sigma_v$  inferred from viscosity and thermal conductivity measurements [26, 74–76] using first order Chapman-Cowling theory [26]. The agreement with our theory for energies below about 1 eV is very good [77] as expected because of our use of long range potentials chosen to be consistent with transport data [42]. The solid circles and squares are obtained by extrapolating the measured elastic  $\sin(\theta)I(\theta)$  [31, 32] data to  $90^\circ$  and then calculating the elastic  $\sigma_v$  using Eq. 4. These points can be compared with the barely discernible dotted curve calculated by assuming that the elastic differential scattering drops to zero at angles greater than that

at which the observed elastic scattering decreases by a factor of 2 [78]. We see that at a collision energy of 1 keV our analysis of the experimental data yields an elastic  $\sigma_v$  value a factor of 30 below the value calculated considering only elastic scattering.

The open circles and squares show the sum  $\sigma_v$  values obtained from the published sum of  $\theta \text{Sin}(\theta)I(\theta)$  data by extrapolating  $\text{sin}(\theta)I(\theta)$  [31, 32] to  $90^\circ$  and then calculating the sum  $\sigma_v$  using Eq. 4. There is considerable uncertainty in the total  $\sigma_v$  values at the higher energies because most of the integrand is obtained using extrapolated data. At a collision energy of 1 keV our analysis of the experimental data yields a sum of elastic and inelastic  $\sigma_v$  cross sections of about 70% of the value calculated considering only elastic scattering.

The dashed curves in figure 5 show our empirical analytical fits to the derived elastic and sum  $\sigma_v$  data. Analytic fits to the various viscosity cross sections are given in the Appendix. Tabulations of the calculated elastic cross sections and analytic fits are available [79].

## IV. NE-NE RESULTS

### A. Ne-Ne interaction potentials

Figure 6 shows representative interaction potentials for the interaction of ground state Ne atoms versus internuclear separation. The potential represented by the solid curve at radii of less than 2.5 bohr is chosen to interpolate smoothly between the theoretical values of Gianturco and Dilonardo [47] at small radii and the recommendation of Aziz and Slaman [80] at large radii. We have shown by points some of the medium-range potentials calculated from theory [47, 81] and potentials inferred from beam scattering experiments [82–85]. Our calculations using Gaussian98 [49] are shown by the solid points. For comparison purposes we have shown the potential calculated for bare Ne nuclei and the potential inferred from  $\text{Ne}^+$  collisions with Ne [50]. At small radii, our potentials are much more repulsive than that of Aziz and Slaman and approach the potential for the bare nuclei. Note that the experimentally based potential of Berry [83] and the theoretically based potential of Abrahamson [81] are considerably above the other data. We have not shown potentials for the excited states of  $\text{Ne}_2$  that approach and/or cross the ground state curve at radii less than  $\approx 2.0$  bohr, but consider their effects on scattering in Sec. IV C.

At the larger radii, there is generally good agreement [80, 86] as to the interaction po-

tential for Ne-Ne internuclear separations larger than 3 au and energies less than 10 eV. We have used the recommendation of Aziz and Slaman rather than the very recent refinements of theoretical potentials [86, 87], which have not been tested against experiment. NOT A VERY GOOD ARGUMENT

### B. Ne-Ne attenuation cross sections

Figure 7 shows beam attenuation cross sections  $\sigma_{att}$  as a function of the angular half-width subtended by the Ne atom detector. The solid curve is calculated by applying Eq. 3 to the elastic differential cross sections calculated using our adopted potential. The experimental attenuation cross sections shown for angles near  $0.1^\circ$  are plotted for effective detector sizes based on our interpretation of the analysis of Amdur and Mason [55, 82]. The data points for detector half-widths above  $30^\circ$  are obtained by integration of  $I(\theta)$  derived from the data of Berry [83]. Note that these results are much larger than the predictions of the elastic scattering theory in spite of the reduction in the attenuation cross section below the elastic scattering values expected at large angles because of inelastic collisions. See Sec. IV C. These large values are consistent with the large values of the interaction potential shown in Fig. 6. POSSIBLY FIGURE 7 SHOULD BE OMITTED AND THE TEXT CHANGED TO SAY THAT THESE DATA SETS ARE USED ELSEWHERE IN THIS SECTION.

### C. Ne-Ne differential cross sections

Differential cross sections for Ne atom-Ne atom collisions expressed in reduced differential cross section form [61] of  $\rho(\tau) = \theta * \text{Sin}(\theta) * I(\theta, E)$  versus  $\tau = \theta * E$  are shown in Fig. 8. The elastic differential cross section from JWKB calculations using our adopted interaction potential from Fig. 6 is shown for a relative energy of 500 eV. The absolute values of the sum of the differential cross sections for elastic and inelastic scattering from the measurements of Berry [83] appear much too large, especially when one considers the expected reduction in magnitude at large angles caused by inelastic effects. See Sec. III C and Fig. 3.

The relative experimental values of  $\rho$  for elastic scattering from Brenot *et al* [32] as fitted to their elastic scattering theory are in good agreement with our theory at small angles where experiment shows that elastic scattering is dominant. The rapid decrease in

the experimental elastic differential cross section beginning at about  $\tau = 5.5$  keV-deg is attributed to the effects of inelastic scattering. The associated energy-loss experiments [32] show that the inelastic collision results principally in the excitation of one atom to the  $2p^53p$  (Paschen notation) configuration at  $\tau$  values  $\leq 6$  keV deg. Weak excitation of atoms to the  $2p^53s$  configuration is observed. At larger  $\tau$  the simultaneous excitation of both atoms to the  $3p$  configuration dominates. This interpretation is confirmed by emission experiments [70, 88] and theory [89], although the details of the reactions proposed by different authors vary. Kempter et al [70] find that the excitation is distributed over about eight of the ten  $2p^53p$  levels. The differential cross sections for ionization are also shown, where the collision products change from an ion plus a ground state atom to an ion plus an excited  $3p$  atom or an ion as  $\tau$  increases [32]. Measurements of photon coincidence rates [88] indicate that about 25% of the excitation events result in two excited atoms. Elastic scattering at large angles is assumed remain small.

Gauyacq [89] calculates reduced differential cross sections for one and two atom excitation of  $Ne(2p^53p)$  in Ne-Ne collisions for collision energies of 500 eV. He obtains rather good agreement with the normalized experimental results of Brenot *et al* [32]. Integrated cross sections are discussed in Secs. IV D and IV E.

#### D. Ne-Ne integrated inelastic cross sections

Figure 9 shows excitation and ionization cross sections for symmetric Ne atom-Ne atom collisions. The curves show the results of representative photon collection experiments [65, 90] and of electron collection experiments by Amme and Haugsjaa [91]. CHECK GAUY-ACQ'S THESIS FOR INTEGRATED THEORETICAL QS. A comparison of experimental and empirical ionization cross sections has been made by Kunc and Soon [38].

???We show the calculated  $Ne(2p^53p)$  excitation cross section of Gauyacq [89] in Fig. 9.??? Because of the identity of target and projectile and the symmetry of the scattering about  $90^\circ$ , we expect the measured total photon or electron-ion production cross sections to be twice the "event" cross sections inferred from theoretical and experimental differential cross section data. See Ref. [64]. The theoretical integrated excitation and ionization cross sections appear to be somewhat larger than the expected half the sum of the 58.4 nm and electron production cross sections shown. The spectra of electrons ejected in Ne-Ne collisions

show autoionization peaks at energies from 14 to 21 eV [69].

Direct excitation of the Ne( $2^3S$ ) metastable states in Ne-Ne collisions appears to occur only when two-electron excitation of the Ne-Ne molecule occurs, followed by dissociation in which both atoms are excited [32, 35] or when one atom is ionized and one is excited [32]. According to Gauyacq [35], excitation of two electrons to the 2s orbital is comparable with single excitation of the 2p orbital and subsequent  $2^1P$  production from threshold to 100 eV, but is smaller at higher energies. However, the fraction leading to direct excitation of  $2^3S$  is apparently unknown. Excitation of  $2^3S$  via cascading from higher levels is roughly an order of magnitude smaller than  $2^1P$  excitation [70]. The data for 587.6 radiation from the  $3^1D$  and subsequent Ne( $2^3S$ ) production is inconsistent between Ref. [65] and Ref. [70]. We have chosen the energy dependence of the former and the magnitude of the latter reference. Theory [35] suggests that excitation of the higher states occurs via the two-electron excitation process.

Direct excitation of the Ne( $2^1S$ ) metastable states in Ne-Ne collisions can occur via excitation of the 1s orbital [34, 35, 37] or when two-electron excitation of the Ne-Ne molecule occurs [35, 37]. Including both processes leads to a somewhat larger  $2^1S$  cross section [35]. The Ne( $2^1S$ ) metastable is produced by cascade excitation from the  $2^1P$  state, but imprisonment of the 58.4 nm resonance radiation is required for efficient metastable production [71]. Additional  $2^1S$  production occurs through cascading from the  $3^1D$  state of Fig. 9.

### E. Ne-Ne transport cross sections

Figure 10 shows total  $\sigma_t$  and viscosity  $\sigma_v$  cross sections for symmetric Ne-Ne collisions. The solid curves are the results of our theory using the potential shown by the solid curve of figure 6. Tabulations are available [79]. The uppermost set of curves and points show the total cross section  $\sigma_t$  as defined in Sec II. The double-dot-dashed line shows that  $\sigma_t$  values calculated using only the long-range, van der Waals interaction [51] and the small angle scattering model of Massey and Mohr [72] are within a factor of two of the detailed theory and experiment. The  $\sigma_t$  points [31, 92] at energies below about 0.1 eV are representative of measurements showing oscillatory structure at very low Ne-Ne collision energies. The  $\sigma_t$  open triangles at above 250 eV show beam attenuation cross sections [82] and are lower limits to the sum of the elastic and inelastic total cross sections.

The lower solid curve in figure ?? is the result of our calculation of the elastic viscosity cross section  $\sigma_v$  using the adopted potential of figure 6. The open circles show viscosity cross sections inferred from our power law fit [77] to viscosity and thermal conductivity measurements [25, 26, 28, 93] using first order Chapman-Cowling theory [26]. The agreement with our theory for energies below about 0.2 eV is very good [77] as expected because of our use of long range potentials chosen to be consistent with transport data [42].

The solid diamond shown at 500 eV is obtained by extrapolating the measured elastic  $\sin(\theta)I(\theta)$  [32] data to  $90^\circ$  and then calculating the elastic  $\sigma_v$  using Eq. 4. This point can be compared with the crosses calculated by assuming that the elastic differential scattering drops to zero at angles greater than that at which the observed elastic scattering decreases by a factor of 2, i.e., a "cut-off" model[78]. For Ne-Ne collisions this cut-off occurs near 5.5 keV deg. The lower dashed curve in figure ?? shows our empirical analytical fit (given in the appendix) to the derived elastic  $\sigma_v$  data. We see that at a collision energy of 500 eV our analysis of the experimental data yields an elastic  $\sigma_v$  value a factor of 25 below the value calculated considering only elastic scattering.

The open diamond shows the sum  $\sigma_v$  value obtained from the published sum of  $\theta\text{Sin}(\theta)I(\theta)$  data by extrapolating  $\sin(\theta)I(\theta)$  [31, 32] to  $90^\circ$  and then calculating the sum  $\sigma_v$  using Eq. 4. The dashed curve through this point shows our empirical analytical fit. It is given in the Appendix. There is considerable uncertainty in the sum  $\sigma_v$  values at the higher energies because most of the integrand is obtained using extrapolated data. At a collision energy of 500 eV our analysis of the experimental data yields a sum of elastic and inelastic  $\sigma_v$  cross sections of about 40% of the value calculated considering only elastic scattering. Tabulations of the calculated elastic cross sections and analytic fits are available [79].

DOES ONE NEED TO ADD A REPRESENTATIVE INELASTIC CROSS SECTION TO FIGURE ???

## V. AR-AR RESULTS

The results presented here for elastic Ar-Ar collisions at low energies follow closely those published recently[94]. At higher energies, the analysis of the effects of inelastic Ar-Ar collisions on the differential and integral cross sections has made use of the simplified models developed in section III to correlate the relatively complete experiments and theory for He-

He collisions.

### A. Ar-Ar interaction potentials

Figure 11 shows representative Ar atom Ar atom interaction potentials versus internuclear separation [71]. Note that the upper portions ( $> 0.0004$  au) of the curves are plotted on a logarithmic scale while the lower portions ( $< 0.0004$  au) are plotted on a linear scale. Also, the internuclear separation  $r$  is plotted on a logarithmic scale to emphasize the data at small radii. The potential represented by the solid curve is chosen to approximate the theoretical values of Gianturco and Dilonardo [47]. The broken curves represent the results of Berry [95], Robinson [96], and the short range potential of Aziz and Slaman [97] as discussed in some detail previously[94]. We have shown by points some of the medium-range potentials calculated from theory [32, 81, 98, 99] and potentials inferred from beam scattering experiments [39, 40, 85, 95, 100]. We see that there is considerable disagreement for separations less than 3 au and energies greater than 10 eV that are of importance for calculations of transport cross sections at collision energies above 100 eV. Not surprisingly, the difference between the adopted potential and the potential calculated for bare nuclei (shown by the dotted line) is larger than for He-He and Ne-Ne.

There is generally good agreement among authors [25, 26, 28, 93, 97, 101] as to the interaction potential for Ar-Ar internuclear separations larger than 3 au and energies less than 10 eV. We have utilized and shown the recommendation of Aziz and Slaman[97, 101].

### B. Ar-Ar attenuation cross sections

Figure 12 shows beam attenuation cross sections  $\sigma_{att}$  as a function of the angular half-width subtended by the Ne atom detector. The solid curve is calculated by applying Eq. 3 to the elastic differential cross sections calculated using our adopted potential. The experimental attenuation cross sections shown for angles near  $0.1^\circ$  are plotted for effective detector sizes based on our interpretation of the analysis of Amdur and Mason [55, 82]. The data points for detector half-widths above  $30^\circ$  are obtained by integration of  $I(\theta)$  derived from the data of Berry [83]. Note that these results are much larger than the predictions of the elastic scattering theory in spite of the reduction in the attenuation cross section below the

elastic scattering values expected at large angles because of inelastic collisions. See Sec. V C. These large values are consistent with the large values of the interaction potential shown in Fig. ??.

### C. Ar-Ar differential cross sections

Figure 13 compares the experimental differential cross section for  $^{40}\text{Ar}$ - $^{40}\text{Ar}$  atoms from Berry [95] (points) with the theoretical results calculated using the Gianturco-Aziz (solid curve) and Berry-Aziz potentials (dot-dash curve) for a collision energy of 1000 eV. The experimental data have been converted to differential cross sections in center-of-mass coordinates. The theoretical results have been averaged over an angle of  $4^\circ$  (FWHM) to simulate the experimental angular resolution. This procedure averages out the large amplitude symmetry oscillations [102] with an apparent period of approximately  $0.2^\circ$ . Figure 13 shows calculated results for asymmetric  $^{38}\text{Ar}$ - $^{40}\text{Ar}$  atom collisions, as well as our empirical fit to theory from section ???. The Berry-Aziz potential gives a significantly better fit of theory to the experimental data than does the Gianturco-Aziz potential. Because of the incomplete analysis of the extended collision geometry of this experiment [95], we place less weight on this agreement and adopt the recently-confirmed theoretical Gianturco and Dilonardo potential at small radii [47, 103]. See section ??.

In this section we consider the contributions of inelastic scattering to the differential cross section for collisions of Ar with Ar. Figure 13 shows our theoretical results and measured differential cross sections for excitation [32] and ionization [104] for a collision energy  $E$  of 1000 eV. We use the reduced differential cross sections ( $\rho = \theta \sin(\theta) d\sigma(\theta, E)/d\theta$ ) versus reduced angle ( $\tau = E\theta$ ) so as to obtain plots that are independent of whether the data is expressed in center-of-mass or laboratory coordinates and are nearly independent of the collision energy at small  $\tau$  [36]. In this type of plot isotropic scattering peaks at  $90^\circ$ . The theoretical  $\rho$  values shown have been smoothed with a Gaussian of  $0.2^\circ$  width (FWHM) to simulate the experimental angular resolution [32, 104]. This greatly reduces the large amplitude symmetry oscillations in the theory.

In figure 13 the measured relative  $\rho$  values Brenot *et al.* [32] are normalized to our theory at small angles where elastic scattering is dominant. Their cross sections measured at 1 keV (CM) have been extended to larger  $\theta$  values using the measurements at 2 keV (CM) [32] and

assuming the validity of the theoretical  $\rho$  versus  $\tau$  scaling [36]. For  $6 < \tau < 25^\circ$  keV the relative values of the neutral atom contribution to  $\rho$  of Eriksen *et al.* [104] are normalized to the sum of the inelastic contributions to  $\rho$  from Brenot *et al.* [32]. The resultant differential cross sections for ionization for  $\tau < 30^\circ$  keV are then extended as shown by the dotted curve so as to yield the integrated ionization cross section of  $2.5 \times 10^{-20}$  m<sup>2</sup> shown in figure 15. Here we assumed that the differential cross section for ionization is symmetrical about  $90^\circ$  in CM and we count ionization events over the entire  $180^\circ$ , just as in the experiments.

The sum of the integrated excitation cross sections from figure 13 is  $3.5 - 5.9 \times 10^{-20}$  m<sup>2</sup> compared to  $\sigma_t^{vuv} = 2.6 \times 10^{-20}$  m<sup>2</sup> from figure 15. Here the uncertainty results from experiments [32] indicating that in some excitation events both colliding atoms are excited. This comparison appears to require a cross section for production of non-radiating excited atoms, i.e., metastables, of  $\sigma_t^{meta} = 1 - 3 \times 10^{-20}$  m<sup>2</sup> at 1000 eV or about equal to the vuv cross section. Metastable atom production has not been detected at these collision energies [105] because of the large ionization background. In figure ?? elastic scattering at large angles is assumed negligible, although Brenot *et al.* [32] say that it rises at large angles.

Departures of the sum of inelastic and elastic scattering differential cross sections from theoretical elastic scattering values when inelastic scattering is large, as in figure ??, have been obtained for collisions between He atoms [32, 54]. From figures ?? and ?? the value of  $\tau \approx 5^\circ$  keV at which the elastic scattering decreases rapidly and the inelastic scattering increases rapidly corresponds to an impact parameter of 2.8 au [32]. This radius is in approximate agreement with the estimated onset of potential curve crossing [32, 65, 104]. The limited and roughly energy-independent range of  $\tau$  and impact parameter over which inelastic scattering is important has been discussed for He<sup>+</sup>-Ne collisions [106] and for H<sup>+</sup>-H<sub>2</sub> collisions [107]. On the basis of the small elastic scattering at large  $\tau$  and large wave-number ( $ka_0 \approx 1600$ ) at 1000 eV, these collisions are analogous to those found for the smooth cut-off, strong-absorption models of nuclear physics [63].

#### D. Ar-Ar integrated inelastic cross sections

Figure 14 shows excitation and ionization cross sections for symmetric Ar atom-Ar atom collisions. The curves the results of representative photon collection experiments [65, 108, 109] and of electron collection (ionization) experiments [105]. Note that the some-

what uncertain cross sections measured for ionization and vuv production very close to the energetic threshold are too small to show in figure 14.

Particularly noteworthy is the virtual equality of the cross sections for vuv production[65, 108–110] and for electron production by ionization[105]. This near equality is much different than for He-He collisions, where the vuv production[65] is large compared to ionization, and for Ne-Ne collisions, where the reported uv production[65] is small compared to ionization. Another way of saying this is that the ionization cross section for He-He collisions is particularly small (BUT WHY NOT EXCITATION?). Empirical ionization cross sections have been discussed by Kunc and Soon [38] and we will not review them here. SUMMARIZE OTHER PAPERS ON RARE GAS IONIZATION.

Direct excitation of the Ar( $3p^54s^3S$ ) metastable states in Ar-Ar collisions appears to occur when two-electron excitation of the Ar-Ar molecule occurs, followed by dissociation in which both atoms are excited [32]. Data is not available when one atom is ionized and one is excited [32]. Excitation of  $3p^54s^3S$  via cascading from higher levels is roughly an order of magnitude smaller than  $3p^54s^1P$  excitation [70]. The data for 587.6 radiation from the  $3p^54s^1D$  and subsequent Ar( $3p^54s^3S$ ) production is inconsistent between Ref. [65] and Ref. [70]. We have chosen the energy dependence of the former and the magnitude of the latter reference.

The chain curve of figure 14 shows the sum of the measured excitation and ionization cross sections. At a collision energy of 1000 eV it is to be compared to the integrated sum of the excitation and ionization cross sections calculated from the differential scattering data shown in figure 13. The ratio of cross sections is somewhat larger than the factor of two expected from the difference in the range of integration angles[111].

### E. Ar-Ar transport cross sections

Figure ?? shows total  $\sigma_t^{th}$  and viscosity  $\sigma_v^{th}$  cross sections for symmetric Ar-Ar collisions. The solid curves are the results of our theory using the potential shown by the solid curve of figure 11. Tabulations are available [79]. The short dashed curves are calculated using the dashed potential energy curve. At low energies we show the total cross section calculated using only the long-range, van der Walls interaction and the small angle scattering model of Massey and Mohr [72]. The points show viscosity cross sections inferred from viscosity and

thermal conductivity measurements [25, 26, 28, 93]. For comparison purposes, we show the accidentally-equal ionization  $\sigma_i$  and vuv excitation  $\sigma_{vuv}$  cross sections [112]. The viscosity cross section proposed by Serikov and Nanbu [10] from an extrapolation of thermal viscosity data is somewhat lower than our result in the 1 to 10 eV range.

## VI. KR-KR RESULTS

### A. Kr-Kr interaction potentials

Figure 16 shows representative Kr atom - Kr atom interaction potentials versus internuclear separation. Again, the upper portions are plotted on a logarithmic scale while the lower portions are plotted on a linear scale, while the internuclear separation  $r$  is plotted on a logarithmic scale. The potential represented by the solid curve is chosen to approximate the theoretical values of Gianturco and Dilonardo [47] at short ranges and the potential recommended by Dharn et al [113]. The chain curve shows the short-range portion of the potential from Dharn et al. We have shown by points some of the medium-range potentials calculated from theory [32, 81, 98, 99] and potentials inferred from beam scattering experiments [40, 114]. We see that there is considerable disagreement for separations less than 3 au and energies greater than 10 eV that are of importance for calculations of transport cross sections at collision energies above 100 eV. In particular, we note that our potential is much more repulsive than that of Dharn et al at small radii.

There is generally good agreement [113] as to the interaction potential for Kr-Kr internuclear separations larger than 3 au and energies less than 10 eV. We have not attempted to test alternate long range potentials [25, 26, 28, 93].

### B. Kr-Kr integrated inelastic cross sections

Figure ?? shows excitation and ionization cross sections for symmetric Kr atom-Kr atom collisions. The curves the results of representative photon collection experiments [65, 108, 109] and of electron collection (ionization) experiments [105]. Note that the somewhat uncertain cross sections measured for ionization and vuv production very close to the energetic threshold are too small to show in figure 14.

### C. Kr-Kr transport cross sections

Figure 17 shows total  $\sigma_t^{th}$  and viscosity  $\sigma_v^{th}$  cross sections for symmetric Kr-Kr collisions. The solid curves are the results of our theory using the potential shown by the solid curve of figure 16. Tabulations are available [79]. The short dashed curves are calculated using the dashed potential energy curve. At low energies we show the total cross section calculated using only the long-range, van der Waals interaction and the small angle scattering model of Massey and Mohr [72]. The points show viscosity cross sections inferred from viscosity and thermal conductivity measurements [25, 26, 28, 93].

## VII. Xe-Xe RESULTS

Figure 18 shows representative Xe atom-Xe atom interaction potentials versus internuclear separation. Note that the upper portions ( $> 0.0004$  au) of the curves are plotted on a logarithmic scale while the lower portions ( $< 0.0004$  au) are plotted on a linear scale. Also, the internuclear separation  $r$  is plotted on a logarithmic scale to emphasize the data at small radii. We have carried out calculations for two interaction potentials that differ for the smaller  $r$  so as to evaluate the corresponding changes in cross sections. The potential represented by the solid curve is chosen to approximate the theoretical values of Gianturco and Dilonardo, [47] and is used in our calculations of elastic scattering. The chain curve shows the short-range portion of the potential recommended by Aziz and Slaman [97, 101] based on the theory of Pathak and Thakar [115]. We have shown by points some of the medium-range potentials calculated from theory [32, 81, 98, 99] and potentials inferred from beam scattering experiments [39, 40, 85, 95, 100]. We see that there is considerable disagreement for separations less than 3 au and energies greater than 10 eV that are of importance for calculations of transport cross sections at collision energies above 100 eV. In particular, we note that our potentials are much more repulsive than that of Aziz and Slaman.

At the larger radii, there is generally good agreement [97, 101] as to the interaction potential for Kr-Kr internuclear separations larger than 3 au and energies less than 10 eV. We have shown the recommendation of Aziz and Slaman and have not attempted to represent or utilize the alternate potentials [25, 26, 28, 93].

Figure 19 shows total  $\sigma_t^{th}$  and viscosity  $\sigma_v^{th}$  cross sections for symmetric Kr-Kr collisions.

The solid curves are the results of our theory using the potential shown by the solid curve of figure 18. Tabulations are available [79]. The short dashed curves are calculated using the dashed potential energy curve. At low energies we show the total cross section calculated using only the long-range, van der Waals interaction and the small angle scattering model of Massey and Mohr [72]. The points show viscosity cross sections inferred from viscosity and thermal conductivity measurements [25, 26, 28, 93]. For comparison purposes, we show the accidentally-equal ionization  $\sigma_i$  and vuv excitation  $\sigma_{vuv}$  cross sections [112].

### VIII. HE-NE RESULTS

### IX. HE-AR RESULTS

### X. NE-XE RESULTS

### XI. DISCUSSION

An aspect of these results that needs to be emphasized is that the common assumption that the cross sections for excitation and ionization can be treated as isotropic scattering with a magnitude equal to the total cross section greatly overestimates the large angle scattering at high collision energies. This approximation is equivalent to assuming that large angle elastic and inelastic scattering at high energies is unimportant in the models (or that atom-atom scattering is unimportant in the overall model). At high energies, the inelastic scattering dominates the sum of the viscosity cross sections and determines the rate of energy transport by fast atoms. Also at high energies, the fractional energy loss is small and inelastic scattering acts a lot like elastic scattering as assumed in the continuous energy loss approximation [? ]. In the case of He-He collisions at 1000 eV, the sum of the inelastic cross sections is  $\sim 1.5 \times 10^{-20} \text{ m}^2$ , whereas we found that the sum of the inelastic viscosity (energy transfer) cross sections is only  $\sim 1.5 \times 10^{-22} \text{ m}^2$ . For Ar-Ar collisions the sum of the inelastic cross sections is  $\sim 5 \times 10^{-20} \text{ m}^2$ , whereas we found that the sum of the inelastic viscosity cross sections is only  $\sim 10^{-21} \text{ m}^2$ .

## Acknowledgments

We thank A. Bogaerts, Z. Donkó, A. Gallagher, C. H. Greene, and L. C. Pitchford for their helpful comments. This work was supported in part by the National Institute of Standards and Technology.

## APPENDIX A: INTERATOMIC POTENTIALS

### 1. Helium

For  $r > 1.2$  bohr our potential  $V(r)$  is

$$V(r) = \epsilon[A^* \exp(-\alpha^* x + \beta^* x^2) - F(x)(c_6/x^6 + c_8/x^8 + c_{10}/x^{10})], \quad (\text{A1})$$

and

$$\begin{aligned} F(x) &= \exp[-\{(D/x) - 1\}^2] \text{ for } x < D \\ &= 1 \text{ for } x > D, \end{aligned} \quad (\text{A2})$$

where  $x = r/r_{min}$ ;  $A^* = 1.86924404 \times 10^5$ ;  $\alpha^* = 10.5717543$ ;  $\beta^* = -2.07758779$ ;  $c_6 = 1.35186623$ ;  $c_8 = 0.414951$ ;  $c_{10} = 0.17151143$ ;  $\epsilon = 0.3469 \times 10^{-5}$ , hartree;  $D = 1.438000$ ; and  $r_{min} = 5.61$  bohr. Here atomic units are used for the radii (1 bohr = 0.529 Å) and potentials (1 hartree = 27.2 eV). The significant figures are those of Ref. [42].

Our fit to the results of Gianturco and Dilonardo [47] for  $r < 1.2$  bohr that patches smoothly on to the larger radii results of Ref. [42] is

$$V(r) = z_1 z_2 / r \exp(-r/r_{scr}), \quad (\text{A3})$$

where the radii and potentials are in atomic units;  $z_1 = z_2 = 1.83$  atomic charges  $r_{scr} = 0.8$  bohr.

### 2. Neon

The Gianturco-Aziz potential shown in figure ?? is described by the Aziz and Slaman formula [97] at larger radii. For  $r > 2.5$  au the potential  $V(r)$  is

$$V(r) = \epsilon(A^* \exp(-\alpha^* x + \beta^* x^2) - F(x)[c_6/x^6 + c_8/x^8 + c_{10}/x^{10}]), \quad (\text{A4})$$

where  $x = r/r_m$ ,  $A^* = 8.9571795e5$ ,  $\alpha^* = 13.86434671$ ,  $\beta^* = -0.12993822$ ,  $c_6 = 1.21317545$ ,  $c_8 = 0.53222749$ ,  $c_{10} = 0.24570703$ ,  $\epsilon = 1.3464e-4$ ,  $D = 1.36$ ,  $r_m = 5.843$ , and

$$\begin{aligned} F(x) &= \exp[-\{(D/x) - 1\}^2] \text{ for } x < D \\ &= 1 \text{ for } x > D. \end{aligned} \quad (\text{A5})$$

For  $r < 2.5$  au our fit to the results of Gianturco and Dilonardo [47] is then

$$V(r) = z_1 z_2 / r^m \exp(-r/ascr), \quad (\text{A6})$$

where  $ascr = 0.62$ ,  $m = 1.2$ ,  $z_1 = 7.2$ , and  $z_2 = 7.2$ .

### 3. Argon

The Gianturco-Aziz potential shown in figure ?? is described by the Aziz and Slaman formula [97] at larger radii. Here the radii and potentials are in atomic units. For  $r > 5$  the potential  $V(r)$  is

$$V(r) = \epsilon[A^* \exp(-\alpha^* x + \beta^* x^2) - F(x)(c_6/x^6 + c_8/x^8 + c_{10}/x^{10})], \quad (\text{A7})$$

where  $\epsilon = 0.3359$ ,  $x = r/r_m$ ,  $r_m = 7.107$ ,  $A^* = 1.13211845 \times 10^5$ ,  $\alpha^* = 9.00053441$ ,  $\beta^* = -2.60270226$ ,  $c_6 = 1.09971113$ ,  $c_8 = 0.54511632$ ,  $c_{10} = 0.39278653$  and

$$\begin{aligned} F(x) &= \exp[-\{(D/x) - 1\}^2] \text{ for } x < D \\ &= 1 \text{ for } x > D. \end{aligned} \quad (\text{A8})$$

Here  $D = 1.00400$  and atomic units are used for the radii (1 au =  $0.529 \times 10^{-10}$  m) and potentials (1 au = 27.2 eV). Here the notation and constants are from [97] with some changes to atomic units.

For  $r < 3$  au our fit to the results of Gianturco and Dilonardo [47] is

$$V(r) = z_1 z_2 / r^{1.5} \exp(-r/0.79). \quad (\text{A9})$$

We use an arbitrary expression to interpolate between equations (A7) and (A9), i.e., if  $3 \leq r \leq 5$  au then

$$V(r) = 2.7(r/2)^{-4.5} \exp[-(r/5.5)^8] / [1 + (r/5.)^4], \quad (\text{A10})$$

where  $z_1 = z_2 = 9.5$  atomic charges. This interpolation visually matches slopes at the patch points.

#### 4. Krypton

#### 5. Xenon

#### 6. He-Xe

#### 7. Ne-Ar

### APPENDIX B: ANALYTIC CROSS SECTIONS

#### 1. Helium

The cross sections  $\sigma$  presented in this Appendix are in  $\text{m}^2$  and the energies  $E$  are collision or relative energies in eV.

For He-He collisions our fit to the integrated elastic or total cross section given by the JWKB calculation is

$$\sigma_t = 3.5 \times 10^{-19} / [1 + (E/35)^2]^{0.15} \quad (\text{B1})$$

For He-He collisions our fit to the elastic viscosity scattering given by the JWKB calculation is

$$\sigma_v^{JWKB} = 6.5 \times 10^{-20} (E)^{-0.17} / [1 + (E/15)^{0.7} + (E/100)^{1.6} + (E/300)^{1.8}] \quad (\text{B2})$$

Our fit to the elastic viscosity scattering based on the experimental differential cross section for elastic scattering is

$$\sigma_v^{elastic} = 6.5 \times 10^{-20} (E)^{-0.17} / [1 + (E/15)^{0.7} + (E/100)^{1.7} + (E/300)^2] / [1 + (E/50)^{2.5}]^{0.4} \quad (\text{B3})$$

Our fit to the sum of elastic and inelastic viscosity scattering based on the experimental differential cross sections is

$$\sigma_v^{sum} = 6.5 \times 10^{-20} (E)^{-0.17} / [1 + (E/15)^{0.7} + (E/100)^{1.7} + (E/300)^2] / [1 + (E/50)^{2.5}]^{0.1} \quad (\text{B4})$$

Our fit to the measured cross section for 501.6 nm excitation by Kempter et al [33, 65] is

$$\sigma^{501.6} = 1.3 \times 10^{-26} (E - 65)^3 / (1 + (E/50)^{2.55}) \quad (\text{B5})$$

for  $E > 65$  eV.

Our fit to the measured cross section for 587.6 nm excitation by Kempter et al [33, 65] is

$$\sigma^{587.6} = 1.6 \times 10^{-21} (1 - \exp[-(E - 85)/150]) (1 + (E/1750)^6)^{0.5}; \quad (\text{B6})$$

for  $E > 85$  eV.

Our fit to the measured cross section for 58.4 nm excitation by Kempter et al [33, 65] is

$$\begin{aligned} \sigma^{58.4} = & 4.4 \times 10^{-26} (E - 20.6)^3 / (1 + (E/50)^{2.85}) \\ & + 4.4 \times 10^{-23} (E - 20.6) / (1 + (E/25)^4) \end{aligned}$$

for  $E > 20.6$  eV.

Our fit to the measured cross section for ionization by Hayden and Utterbak [67] is

$$\sigma^{ion} = 2.3 \times 10^{-25} E^{1.23} (1 - \exp[-(E - 52)/10]) \quad (\text{B7})$$

for  $E > 52$  eV.

## 2. Neon

For Ne-Ne collisions our fit to the integrated elastic or total cross section given by the JWKB calculation is

$$\sigma_t = 3.5 \times 10^{-19} / [1 + (E/35)^2]^{0.055} [1 + (0.7/E)^1]^{0.47} / [1 + (.012/E)^2]^{0.6} \quad (\text{B8})$$

For Ne-Ne collisions our fit to the elastic viscosity cross section given by the JWKB calculation is

$$\sigma_v^{JWKB} = 9.8 \times 10^{-20} E^{-0.17} / [1 + 0.7(E/100)^{0.5} + (E/450)] [1 + (.017/E)^5]^{0.1} \quad (\text{B9})$$

Our fit to the elastic viscosity scattering based on the experimental elastic differential scattering

$$\sigma_v^{elastic} = 9.0 \times 10^{-20} E^{-0.2} / [1 + 0.7(E/100)^{0.5} + (E/50)^{4.6}]^{0.4} [1 + (.017/E)^5]^{0.1} \quad (\text{B10})$$

Our fit to the sum of elastic and inelastic viscosity scattering based on the experimental differential cross sections is

$$\sigma_v^{sum} = 9.8 \times 10^{-20} E^{-0.17} / [1 + 1.4 * (E/100)^{0.5} + (E/50)^2]^{0.5} [1 + (.017/E)^5]^{0.1} \quad (\text{B11})$$

### 3. Argon

The Ar-Ar cross section for total scattering  $\sigma_t$  obtained by fitting the theoretical values shown in figure 15 is given by

$$\sigma_t = 2.1 \times 10^{-18} E^{-0.4} [1 + (E/15)^2]^{0.16} \quad (\text{B12})$$

Our fit to the elastic viscosity cross section for Ar-Ar collisions from the JWKB calculation is

$$\sigma_v^{JWKB} = 17. \times 10^{-20} (E)^{-0.17} / [1 + 0.8(E/100)^{0.5} + (E/450)^{0.75}] [1 + (.06/E)^5]^{0.1} / [1 + (.02/E)^5]^{0.1} \quad (\text{B13})$$

Our fit to the elastic scattering based on the experimental elastic scattering is

$$\sigma_v^{elastic} = 17. \times 10^{-20} (E)^{-0.17} / [1 + 3.0(E/100)^{0.5} + (E/45)^5]^{0.4} [1 + (.06/E)^5]^{0.1} / [1 + (.02/E)^5]^{0.1} \quad (\text{B14})$$

Our fit to the sum of elastic and inelastic scattering based on the experimental differential cross sections is

$$\sigma_v^{sum} = 17. \times 10^{-20} (E)^{-0.17} / [1 + 3.0(E/100)^{0.5} + (E/45)^{3.2}]^{0.4} [1 + (.06/E)^5]^{0.1} / [1 + (.02/E)^5]^{0.1} \quad (\text{B15})$$

---

[1] H. Neu, Z. Phys. **155**, 77 (1959).

[2] See, for example, D. G. Armour, H. Valisadeh, F. A. H. Soliman and G. Carter, Vacuum **34**, 295 (1984).

- [3] D. A. Scott and A. V. Phelps, Phys. Rev. A **43**, 3043 (1991).
- [4] K. N. Ul'yanov and A. B. Tskhai, Tepolfiz. Vys. Temp. **19**, 41 (1981)[Engl. Trans. High Temp. (USSR) **19**, 32 (1981)].
- [5] E. J. Lauer, S. S. Yu and D. M. Cox, Phys. Rev. A **23**, 2250 (1981).
- [6] J. Rickards, Vacuum **34**, 559 (1984).
- [7] A. Kersch, W. Morokoff and Chr. Werner, J. Appl. Phys. **75**, 2278 (1994).
- [8] R. S. Mason and R. M. Alott, J. Phys. D: Appl. Phys. **27**, 2372 (1994).
- [9] A. Bogaerts, M. van Straaten and R. Gijbels, Spectrochim. Acta **50B**, 179 (1995).
- [10] V. V. Serikov and K. Nanbu, J. Vac. Sci. Technol. A **14**, 3108 (1996).
- [11] A. V. Phelps and Z. Lj. Petrović, Plasma Sources Sci. Tech. **8**, R21 (1999).
- [12] G. W. McClure, J. Electron. Control **7**, 439 (1959).
- [13] P. Hartman, Z. Donkó, G. Bánó, L. Szalai and K. Rózsa, Plasma Sources Sci. and Technol. **9**, 183 (2000).
- [14] D. Y. Oh, D. E. Hastings, C. M. Marrese, J. M. Haas, and A. D. Gallimore, J. Propulsion and Power, **15**, 345 (1999).
- [15] A. Bogaerts, Plasma Sources Sci. Technol. **8**, 210 (1999).
- [16] Z. Donkó, J. Appl. Phys. **88**, 2226 (2000).
- [17] I. Revel, L. C. Pitchford and J. P. Boeuf, J. Appl. Phys. **88**, 2234 (2000).
- [18] G. J. M. Hagelaar, G. M. W. Kroesen, and M. H. Klien J. Appl. Phys. **88**, 2240 (2000).
- [19] H. Capdeville, C. Pédoissant, and L. C. Pitchford J. Appl. Phys. **91**, 1026 (2002).
- [20] G. Bánó, L. Szalai, P. Horváth, K. Kutasi, Z. Donkó, K. Rózsa, T. M. Adamowicz, J. Appl. Phys. **??**, ???? (2002).
- [21] M. J. Jamieson, A. Dalgarno and J. N. Yukich, Phys. Rev. A **46**, 6956 (1992).
- [22] R. Celiberto, U. T. Lamanna, and M. Capitelli Phys. Rev. A **58**, 2106 (1998).
- [23] P. S. Krstić and D. R. Schultz, J. Phys. B: At. Mol. Opt. Phys. **32**, 3485 (1999).
- [24] G. A. Bird, *12th International Symposium on Rarefied Gas Dynamics* (Am. Inst. of Aeronautics and Astronautics, New York, 1980) p 239.
- [25] J. O. Hirshfelder, C. F. Curtiss and B. B. Bird, *Molecular Theory of Gases and Liquids* (Wiley, New York, 1954) ch 8.
- [26] S. Chapman and T. G. Cowling *The Mathematical Theory of Non-Uniform Gases* (University Press, Cambridge, 1970) ch 12 and 13.

- [27] N. F. Mott and H. S. W. Massey, *The Theory of Atomic Collisions* (Clarendon, Oxford, 1965) 3rd ed ch 2, 3 and 8.
- [28] J. H. Dymond, *J. Phys. B: Atom. Molec. Phys.* **4**, 621 (1971).
- [29] R. A. Aziz, *J. Thermophys.* **8**, 193 (1987).
- [30] M. Barat, D. Dhuicq, R. François, C. Lech, and R. Mc Carroll, *J. Phys. B: At. Mol. Opt. Phys.* **6**, 1206 (1973).
- [31] R. Morgenstern, M. Barat, and D. C. Lorents, *J. Phys. B: At. Mol. Opt. Phys.* **6**, L330 (1973).
- [32] J. C. Brenot, D. Dhuicq, J. P. Gauyacq, J. Pommier, V. Sidis, M. Barat and E. Pollack, *Phys. Rev. A* **11**, 1245 (1975).
- [33] V. Kempter, in *The Physics of Electronic and Atomic Collisions*, ed by J. S. Risley and R. Geballe, (Univ. Washington Press, 1975, Seattle), p.327.
- [34] R. E. Olson, E. J. Shipsey, and J. C. Browne, *J. Phys. B: At. Mol. Opt. Phys.* **8**, 905 (1975).
- [35] J. P. Gauyacq, *J. Phys. B* (9) **3067** (1976).
- [36] F. T. Smith, R. P. Marchi and K. G. Dedrick, *Phys. Rev.* **150**, 79 (1966).
- [37] J. P. Gauyacq, *J. Phys. B* **9** 2289 (1976).
- [38] J. A. Kunc and W. H. Soon, *J. Chem. Phys.* **95**, 5738 (1991).
- [39] I. Amdur and E. A. Mason, *J. Chem. Phys.* **22**, 670 (1954).
- [40] I. Amdur, J. E. Jordan and R. R. Bertrand, in *Atomic Collisions Processes* (North-Holland, Amsterdam, 1964) p 934.
- [41] A. V. Phelps, *J. Appl. Phys.* **76**, 747 (1994).
- [42] R. A. Aziz, A. R. Janzen and M. R. Moldover, *Phys. Rev. Lett.* **74**, 1586 (1995).
- [43] A. R. Janzen and R. A. Aziz, *J. Chem. Phys.* **107**, 914 (1997).
- [44] J. E. Jordan and I. Amdur, *J. Chem. Phys.* **46**, 165 (1967).
- [45] P. B. Forman, P. K. Rol and K. P. Coffin, *J. Chem. Phys.* **61**, 1658 (1974).
- [46] A. A. Abrahamson, *Phys. Rev.* **178**, 76 (1969).
- [47] F. A. Gianturco and M. Dilonardo, *J. Chim. Phys.* **72** 315 (1975).
- [48] D. M. Ceperley and H. Partridge, *J. Chem. Phys.* **84**, 820 (1986).
- [49] Gaussian98 (Revision A.7), M. J. Frisch et al, Gaussian, Inc., Pittsburgh PA, 1998. Potentials were obtained using MethodQCID and Basis 6-31G(d).
- [50] G. H. Lane and E. Everhardt, *Phys. Rev.* **120**, 2064 (1960).

- [51] E. W. McDaniel, J. B. A. Mitchell, and M. E. Rudd, *Atomic Collisions: Heavy Particle Projectiles* (Wiley, New York, 1993) ch 1.
- [52] ?????appears to be He-He excited state potentials ???????????
- [53] Krstić P S and Schultz D R 1999 Phys. Rev. A. 60 2118
- [54] J. H. Newman, K. A. Smith, and R. F. Stebbings, J. Geophys. Res. 90, 11,045 (1985).
- [55] I. Amdur and A. L. Harkness, J. Chem. Phys. 22, 664 (1954).
- [56] I. Amdur, J. E. Jordan, and S. O. Colgate, J. Chem. Phys. 34, 1525 (1961).
- [57] Y. N. Belyaev and V. B. Leonas, Dokl. Akad. Nauk. SSSR 173, 306 (1967)[Sov. Phys. - Dokl. 12, 233 (1967)].
- [58] W. J. Savola Jr., F. J. Eriksen, and E. Pollak, Phys. Rev. A 7, 932 (1973).
- [59] D. E. Nitz, R. S. Gao, L. K. Johnson, K. A. Smith, and R. F. Stebbings, Phys. Rev. A 35, 4541 (1987).
- [60] D. N. Ruzic and S. A. Cohen, J. Chem. Phys. 83, 5527 (1985).
- [61] Reduced differential cross sections are commonly used so as to obtain plots that are nearly independent of the collision energy, as is predicted for small  $\tau$  [36]. An incidental advantage of these plots is that they are the same for laboratory-frame data and for center-of-mass data.
- [62] E. W. McDaniel, *Collision Phenomena in Ionized Gases* (Wiley, New York, 1964) ch 1.
- [63] G. R. Satchler *Introduction to Nuclear Reactions* (Oxford, New York, 1990) ch 4.
- [64] This factor of two results from the conventions for defining cross sections for symmetric particle collisions. In measurements or calculations of the flux of inelastically scattered particles the cross section is limited by the equivalent of an integration over the inelastic differential scattering cross section from 0 to 90° in center-of-mass, so as not to count the same collision event twice. The conventional UV photon or electron collection experiments used to determine excitation and ionization cross sections measure photon or electron-ion fluxes produced by particles scattered through all angles, i.e., from 0 to 180°. Because of the symmetry of the scattering about 90°, the second cross section is twice the first. For a brief discussion of this effect see, for example, Sec. 9 of W. E.

- Frahn and K. E. Rehm, *Phys. Reports* 37C, 1 (1978). These arguments show that that the normalized experimental excitation cross sections shown in Ref. [33] and Ref. [35] and the normalized ionization cross sections shown in Ref. [35] are too small by a factor of two. Thus, the integral cross sections of Gauyacq [35] agree well with experiments.
- [65] V. Kempter, F. Veith, and L. Zehnle, *J. Phys. B: Atom. Molec. Phys.* 8, 1041 (1975).
- [66] Because a sodium salicylate scintillator is used to convert all extreme uv to visible, the wavelength of the uv emission is not determined.
- [67] H. C. Hayden and N. G. Utterbak, *Phys. Rev.* 135, A1575 (1964).
- [68] Another factor causing the cut-off model to overestimate the sum of the inelastic cross sections is decrease in the inelastic differential cross sections with increasing scattering angle.
- [69] G. Gerber, R. Morgenstern, and A. Niehaus, *J. Phys. B* 6, 493 (1973).
- [70] V. Kempter, G. Riecke, F. Veith, and L. Zehnle, *J. Phys. B: Atom. Molec. Phys.* 9, 3081 (1976).
- [71] Our analysis suggests that the Doppler shift of the resonance line emission from the fast He( $2^1P$ ) atoms produced in the collisions of fast He with He is sufficient to allow the resonance photons to reach the walls without absorption for Torr-cm size plasmas.
- [72] H. S. W. Massey and C. B. O. Mohr, *Proc. Roy. Soc. (London)* A144, 188 (1934).
- [73] R. Feltgen, H. Pauly, F. Torello, and H. Vehmeyer, *Phys. Rev. Lett.* 30, 820 (1973).
- [74] S. C. Saxena, *High Temp. Sci.* 3, 168 (1971).
- [75] A. Acton and K. Kellner, *Physica (Utrecht)* 90B, 192 (1977).
- [76] E. Vogel, *Ber. Bunsenges. Phys. Chem.* 88. 997 (1984).
- [77] The deviations of these points from the theoretical curve are in the direction expected from the deviations of the measured viscosity from our simple power-law fit to experimental viscosities (not shown).
- [78] This calculation utilized an analytical fit to slowly varying measured "cutoff" angles and the apparent threshold found experimentally and shown for the exci-

tation and ionization cross sections. It is to be noted [117] that for small scattering angles a constant cutoff  $\tau$  value for the onset of inelastic effects corresponds to a constant value of the distance of closest approach of the colliding atoms, e.g., the internuclear separation of crossing of ground state and excited state potential energy curves. The tendency for a decrease in the cutoff tau with increasing collision energy suggests the onset of nonadiabatic effects. SHOULD THIS SPECULATION BE DELETED? Typical cutoff values in deg-keV for various collision pairs are: He-He, 3; Ne-Ne, 5.5; Ar-Ar, 4.8.

- [79] A. V. Phelps *ftp://jila.colorado.edu/collision\_data/readme.txt* (unpublished).
- [80] R. A. Aziz and M. J. Slaman, *Chem. Phys.* 130 187 (1989).
- [81] A. A. Abrahamson, *Phys. Rev.* 130, 693 (1963).
- [82] I. Amdur and E. A. Mason, *J. Chem. Phys.* 23 415 (1955).
- [83] H. W. Berry, *Phys. Rev.* 99 553 (1955).
- [84] P. E. Siska, J. M. Parson, T. P. Schafer and Y. T. Lee *J. Chem.Phys.* 55, 5762 (1971).
- [85] As cited in Appendix 2.B of R. A. Aziz, in *Inert Gases* edited by M. L. Klein (Springer-Verlage, 1984, Berlin).
- [86] S. M. Cybulski, R. R. Toczyłowski, *J. Chem. Phys.* 111 10520 (1999).
- [87] R. J. Gdanitz, *Chem. Phys. Lett.* 348 67 (2001).
- [88] P. J. Martin, G. Riecke, J. Hermann, L. Zehnle, and V. Kempter, *J. Phys. B* 11, 1991 (1978).
- [89] J. P. Gauyacq, *J. Phys. B* 11, 85 (1978).
- [90] N. H. Tolk, C. W. White, S. H. Dworesky, and D. L. Simms, in *Proc. 7th Int. Conf. on Physics of Electronic and Atomic Collisions* ed. by L. M. Branscomb *et al* (North-Holland, Amsterdam, 1971), p584.
- [91] R. C. Amme and P. O. Haugsjaa and *Phys. Rev.* 177, 230 (1969).
- [92] B. Brunetti, F. Pirani, F. Vecchiocattivi, and E. Luzzatti, *Chem. Phys. Lett.* 58, 504 (1978).
- [93] R. N. Keeler, M. Van Theil and B. J. Adler, *Physica (Utrecht)* 31, 1437 (1965).
- [94] A. V. Phelps, C. H. Greene, and J. P. Burke, Jr., *J. Phys. B* 33, 2965 (2000).
- [95] H. W. Berry, *Phys. Rev.* 75, 913 (1949).

- [96] R. S. Robinson, *J. Vacuum Sci Tech.* 16 185 (1979).
- [97] R. A. Aziz and M. J. Slaman, *J. Chem. Phys.* 92, 1030 (1990).
- [98] F. T. Smith, *Phys. Rev.* 179, 111 (1972).
- [99] R. G. Gordon and Y. S. Kim, *J. Chem. Phys.* 56, 3122 (1972).
- [100] S. O. Colgate, J. E. Jordan, I. Amdur and E. A. Mason, *J. Chem. Phys.* 51, 968 (1969).
- [101] R. A. Aziz, *J. Chem. Phys.* 99, 4518 (1993).
- [102] J. M. Parson, P. E. Siska and Y. T. Lee *J. Chem. Phys.* 56, 1511 (1972).
- [103] E. L. Hamilton and C. H. Greene (unpublished) (1999). Calculation for Ar-Ar carried out using Gaussian98, MethodQCID, and Basis 6-31G(d)).
- [104] F. J. Eriksen, S. M. Fernandez, A. B. Bray and E. Pollack, *Phys. Rev. A* 11, 1239 (1975).
- [105] P. O. Haugsjaa and R. C. Amme *J. Chem. Phys.* 52, 4874 (1970).
- [106] J. Baudon, M. Barat and M. Abignoli, *J. Phys. B: Atom. Molec. Phys.* 3, 207 (1970).
- [107] M. Baer, G. Nieder-Shatteburg, and J. P. Toennies, *J. Chem. Phys.* 91, 4169 (1989).
- [108] H. L. Rothwell, Jr., R. C. Amme, and B. Van Zyl, *Phys. Rev. Lett.* 36, 785 (1976).
- [109] P. O. Haugsjaa and R. C. Amme, *Phys. Rev. Lett.* 23, 633 (1969).
- [110] H. L. Rothwell, Jr., R. C. Amme, and B. Van Zyl, *Phys. Rev. A* 19, 970 (1979).
- [111] ?????????????? Another factor causing the cut-off model to overestimate the sum of the inelastic cross sections is decrease in the inelastic differential cross sections with increasing scattering angle.
- [112] A. V. Phelps *J. Phys. Chem. Ref. Data* 20, 557 (1991).
- [113] A. K. Dham, A. R. Allnatt, W. J. Meath, and R. A. Aziz, *Mol. Phys.* 67, 129 (1989).
- [114] From Table 7 of appendix 2.B of R. A. Aziz, in "Inert Gases", ed. by M. L. Klein (Springer-Verlag, New York, 1984). See also [113].
- [115] R. K. Pathak and A. J. Thakkar *J. Chem. Phys.* 87, 2186 (1987).
- [116] Krstić P S and Schultz D R 1999 *J. Phys. B: At. Mol. Opt. Phys.* 32 2415

[117] E. Everhardt, *Phys. Rev.* **132**, 2083 (1963).

[118] P. B. Foreman and P. K. Rol Bull. Am. Phys. Soc. **18**, 378 (1973).

[119] ????????????????

[120] ????????????????

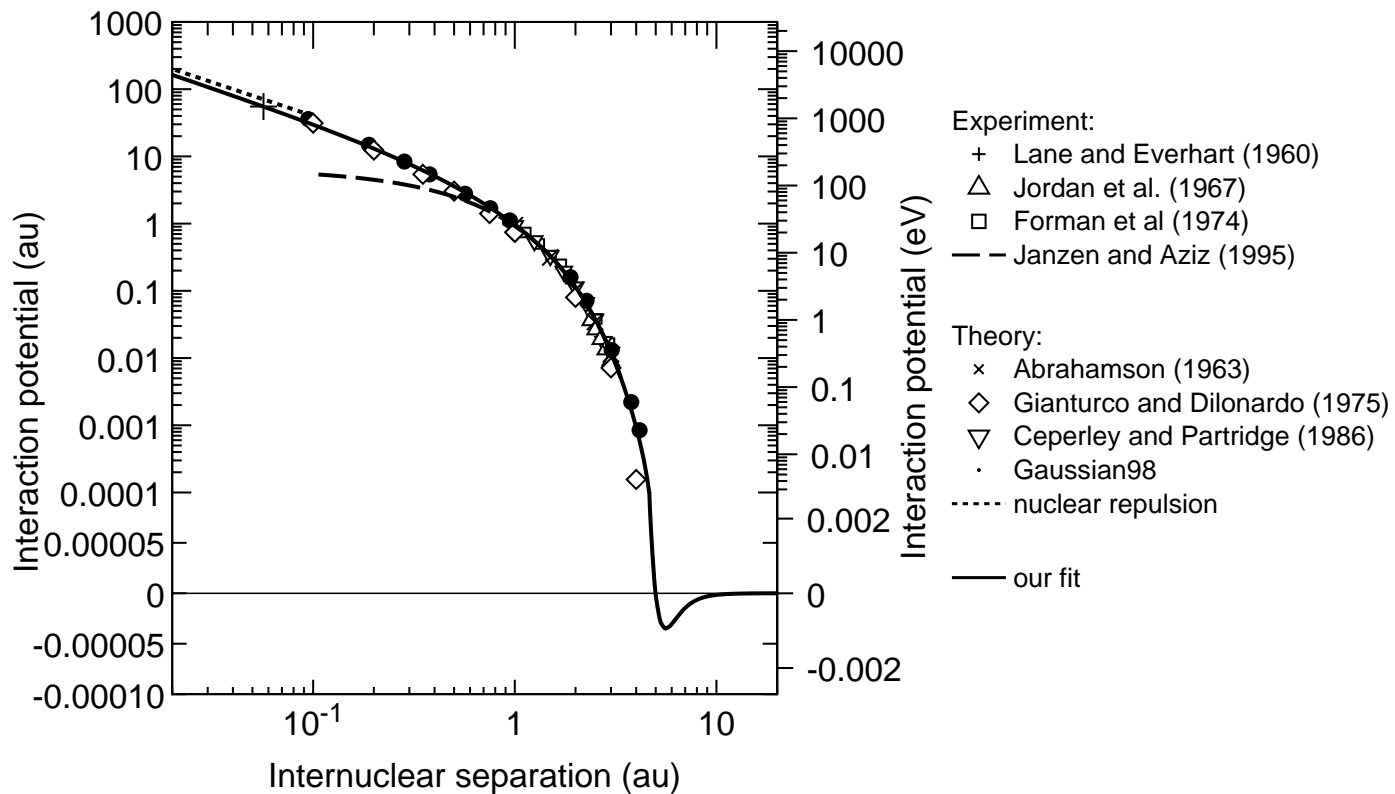


FIG. 1: Interaction potentials versus internuclear separation for He atoms with emphasis on the smaller radii. Note that the upper portion of the curves is plotted on a logarithmic scale while the lower portion is plotted on a linear scale. The solid curve shows our adopted interaction potential, which agrees with the recommendation of Aziz et al [42] except as shown by the short dashed portion. Some results of theories are shown by the symbols and references:  $\times$  [46];  $\diamond$ , [47];  $\circ$ , [49];  $\nabla$ , [48]. Potentials derived from scattering experiments are shown by the symbols and references:  $\triangle$ , [44]; and  $\square$  [45].

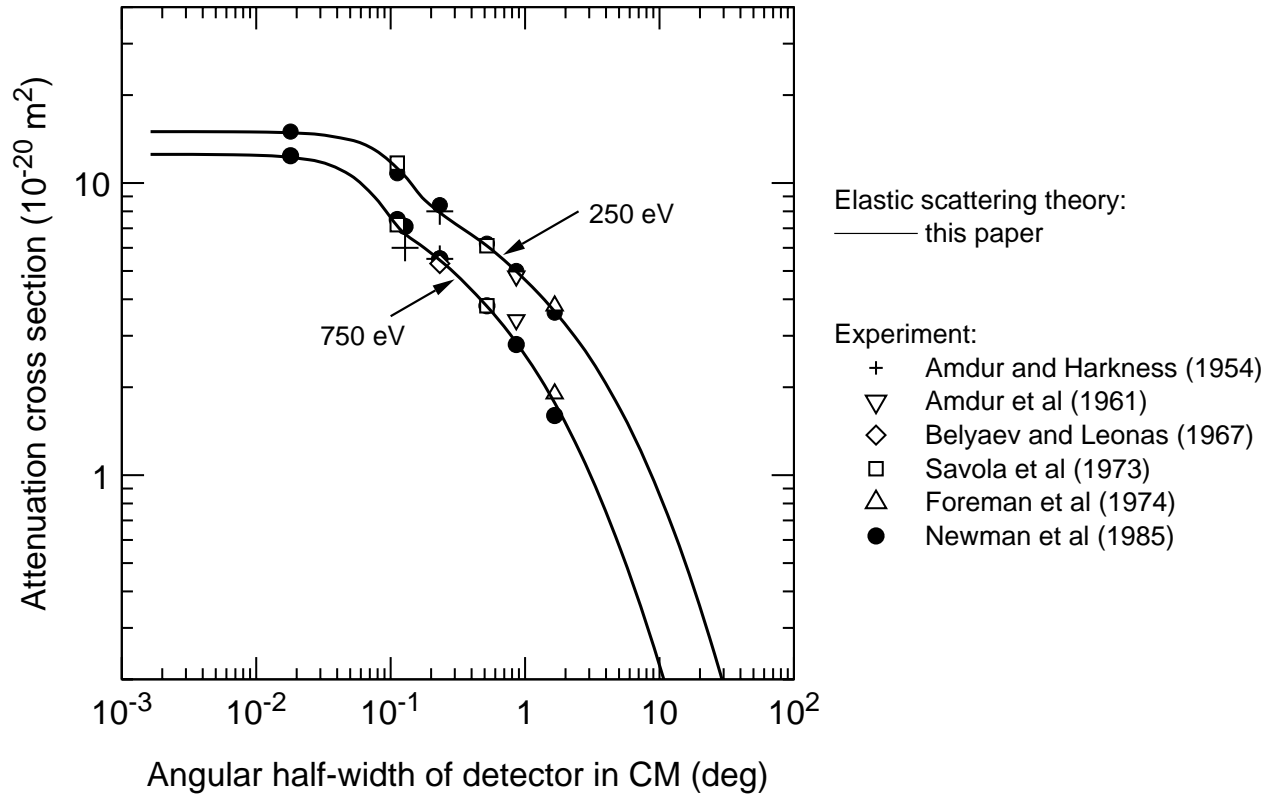


FIG. 2: Attenuation cross sections  $\sigma_{att}$ , for symmetric He atom-He atom collisions at 250 and 750 eV in CM. The solid curves show the results of our calculations of elastic scattering using the interaction potentials shown by the solid curves of figure 1. The symbols and associated references are: + [55];  $\nabla$ , [56];  $\diamond$ , [57];  $\square$ , [58];  $\triangle$ , [45]; and  $\bullet$ , [54].

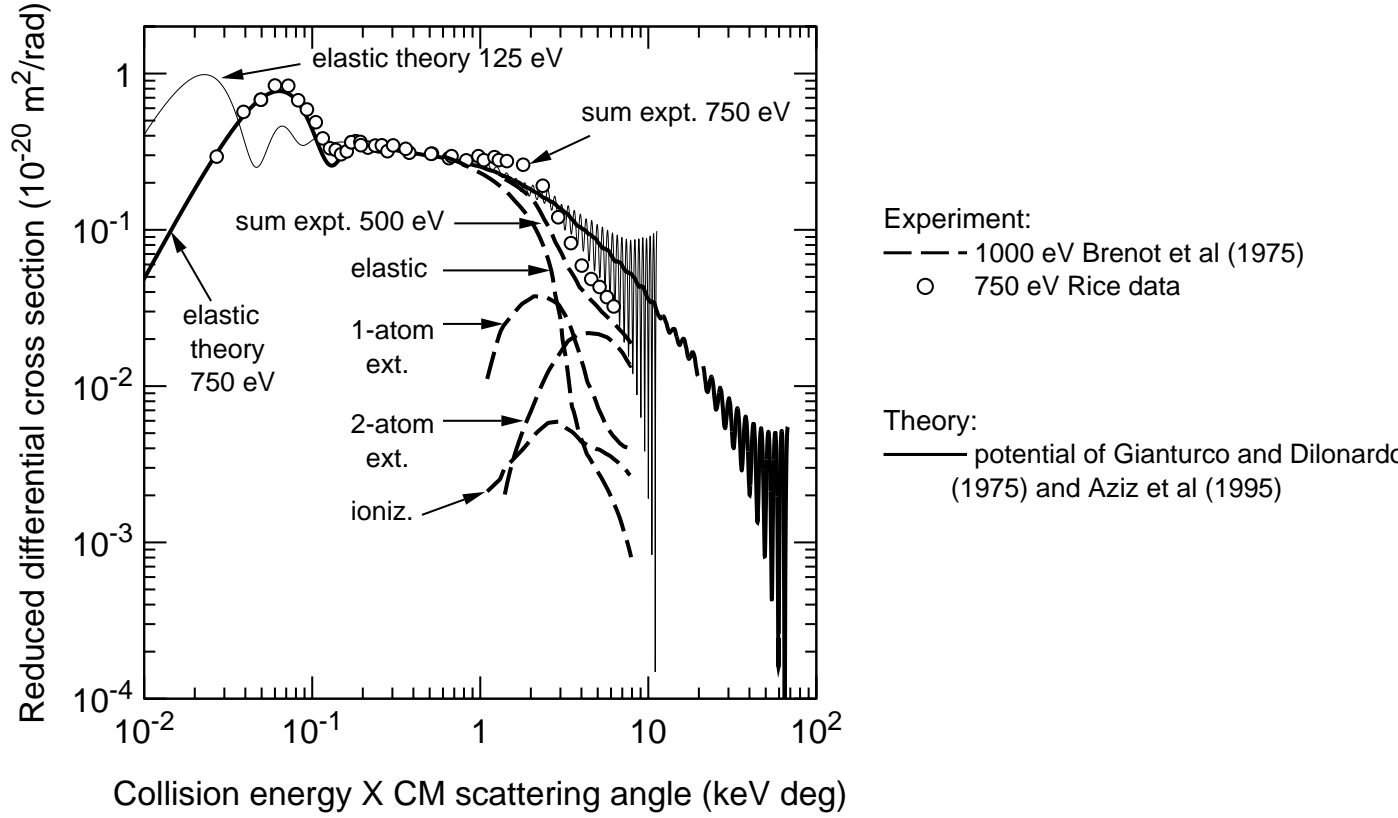


FIG. 3: Differential cross sections for symmetric He atom-He atom collisions expressed in normalized form of  $\rho = \theta * \text{Sin}(\theta) * I(\theta, E)$  versus  $\tau = \theta * E$ . The solid curve are the results of our JWKB calculations using the interaction potentials shown by the solid curve of figure 1. The points show the experimental sum for all scattering processes from the Rice experiments [54, 59] for a relative energy of 750 eV. The dashed curves are the renormalized results by Brenot et al [31, 32] for the sum of all processes and for the dominant elastic and inelastic processes for a relative energy of 1000 eV.

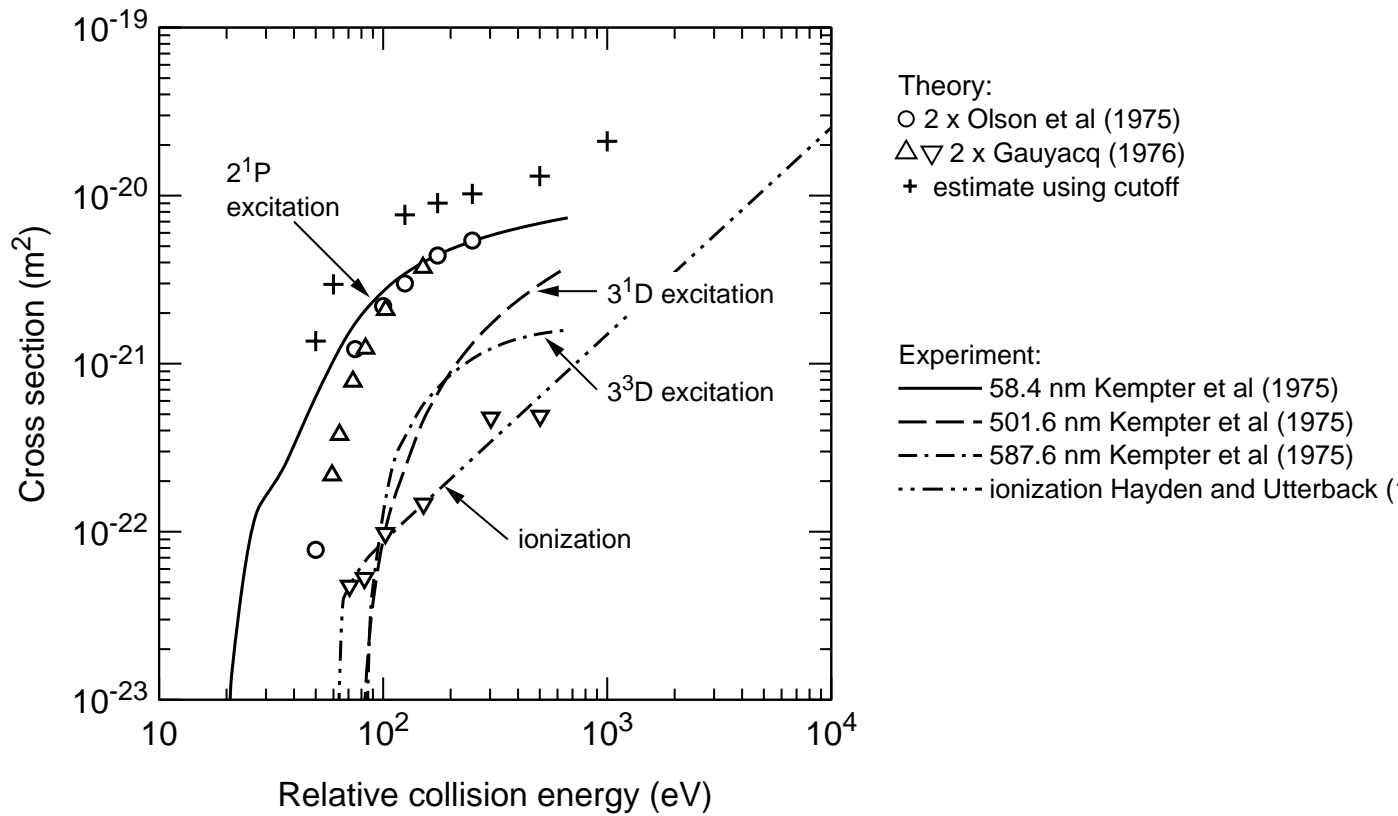


FIG. 4: Angle integrated excitation and ionization sections for symmetric He atom-He atom collisions. The curves show the results of photon and electron collection experiments integrated over 0 to 180 ° in center of mass. The points show theory with the same range of angle integration. See text for explanation. The symbols and associated references are: □ [31]; ○, [34]; △,▽, [35]; 2<sup>1</sup>P, 3<sup>1</sup>D, 3<sup>3</sup>D [65]; and — - - , [67].

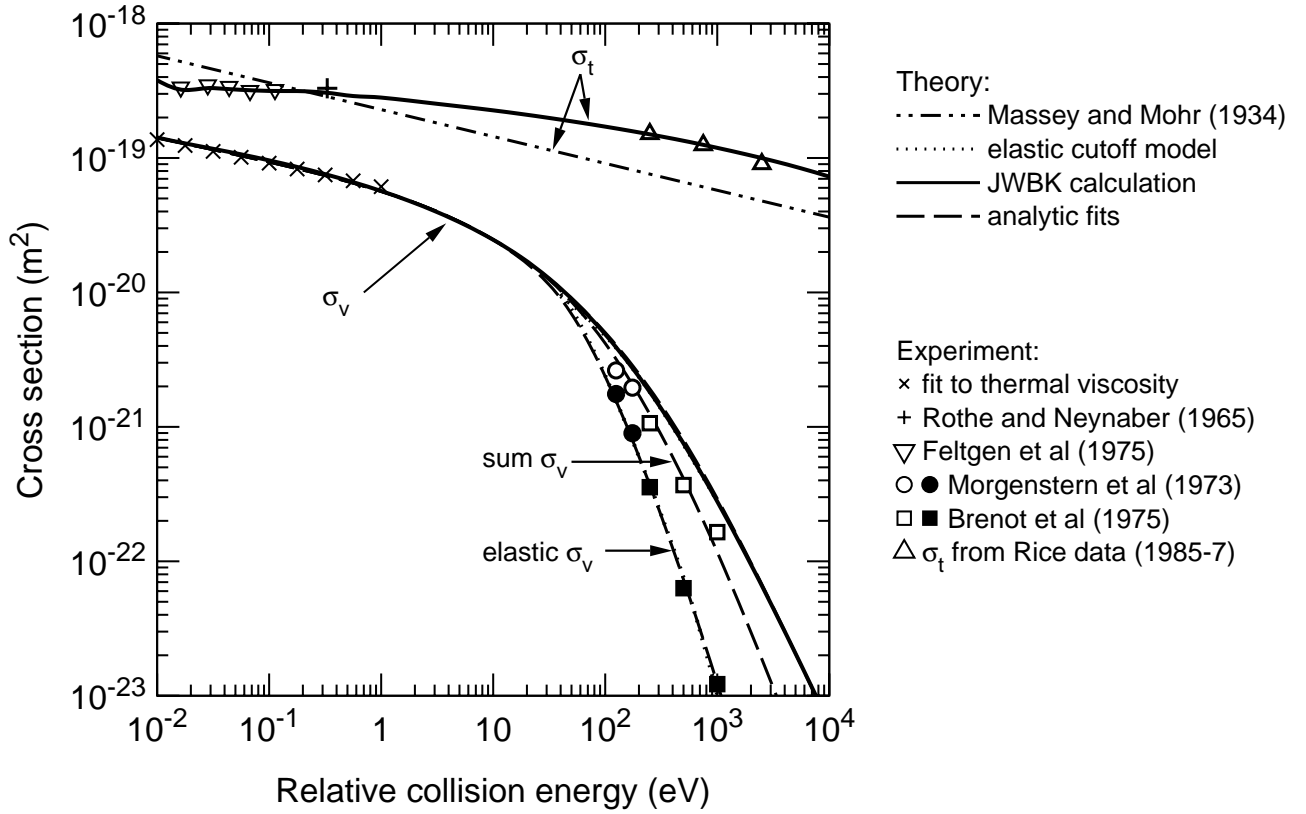


FIG. 5: Total  $\sigma_t$ , viscosity  $\sigma_v$ , and inelastic cross sections for symmetric He atom-He atom collisions. The solid curves show the results of our calculations of elastic scattering using the interaction potentials shown by the solid and dashed curves of figure 1. The chain curve is the total cross section from the long-range potential model of Massey and Mohr [72]. The points are viscosity cross sections inferred from viscosity and thermal conductivity measurements, as discussed in the text. The dashed curves show our analytical fits to the various viscosity cross sections.

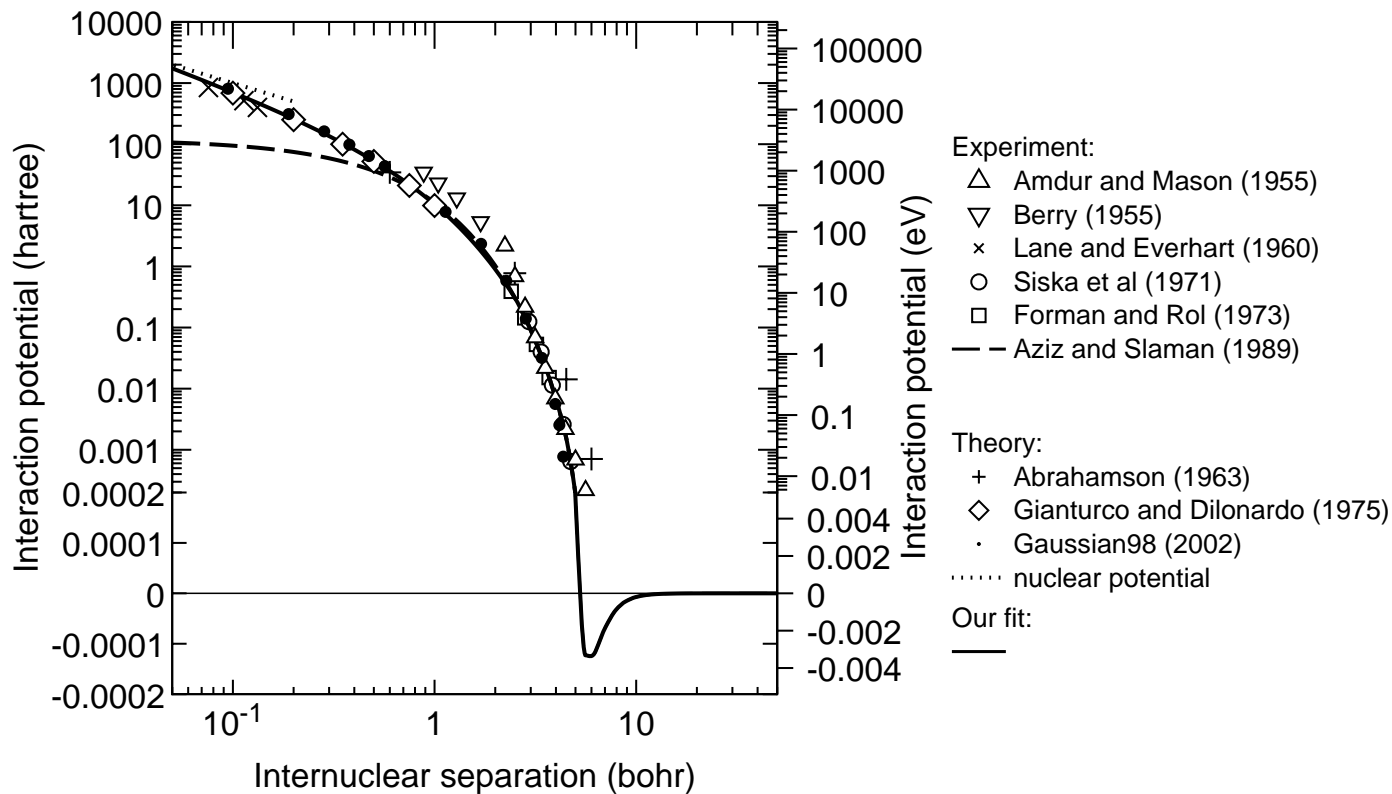


FIG. 6: Interaction potentials versus internuclear separation for Ne atoms with emphasis on the smaller radii. Note that the upper portion of the curves is plotted on a logarithmic scale while the lower portion is plotted on a linear scale. The solid curve shows our adopted interaction potential. The dashed curve shows the recommendation of Aziz and Slaman [80]. Some results of theories are shown by the symbols and references: + [81]; ◇, [47]; and •, [49]. Some potentials based on experiment are shown by the symbols and references: △, [82]; ▽, [83]; ×, [50]; ○, [84]; □, [118]; and — — [80]. The potential for bare Ne nuclei is shown by the dotted line

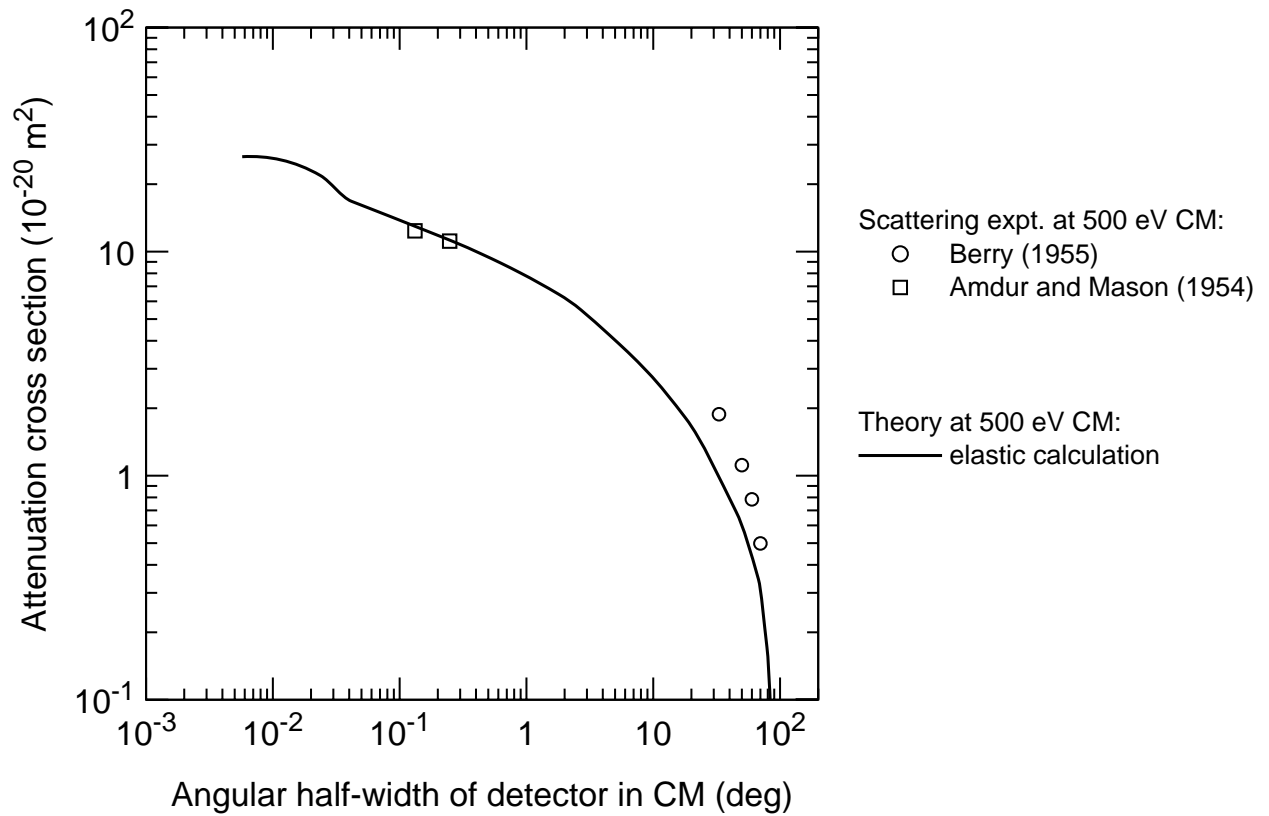


FIG. 7: Attenuation cross sections  $\sigma_{att}$  for symmetric Ne atom-Ne atom collisions at 250 and 750 eV in CM. The solid curves show the results of our calculations of elastic scattering using the interaction potentials shown by the solid curves of figure 6. The symbols and associated references are: + [55];  $\nabla$ , [56];  $\diamond$ , [57];  $\square$ , [58];  $\triangle$ , [45]; and  $\bullet$ , [54].

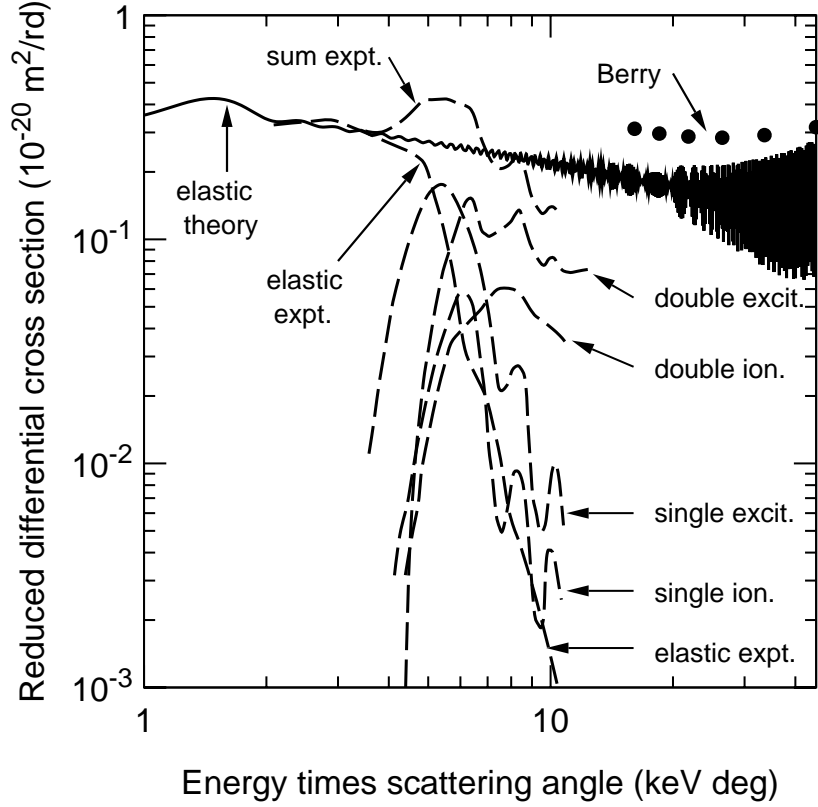


FIG. 8: Differential cross sections for symmetric Ne atom-Ne atom collisions expressed in normalized form of  $\rho = \theta * \text{Sin}(\theta) * I(\theta, E)$  versus  $\tau = \theta * E$ . The solid curve are the results of our JWKB calculations using the interaction potentials shown by the solid curve of figure 6. The points show the experimental sum for all scattering processes from the Rice experiments [54, 59] for a relative energy of 750 eV. The dashed curves are the renormalized results by Brenot et al [31, 32] for the sum of all processes and for the dominant elastic and inelastic processes for a relative energy of 1000 eV.

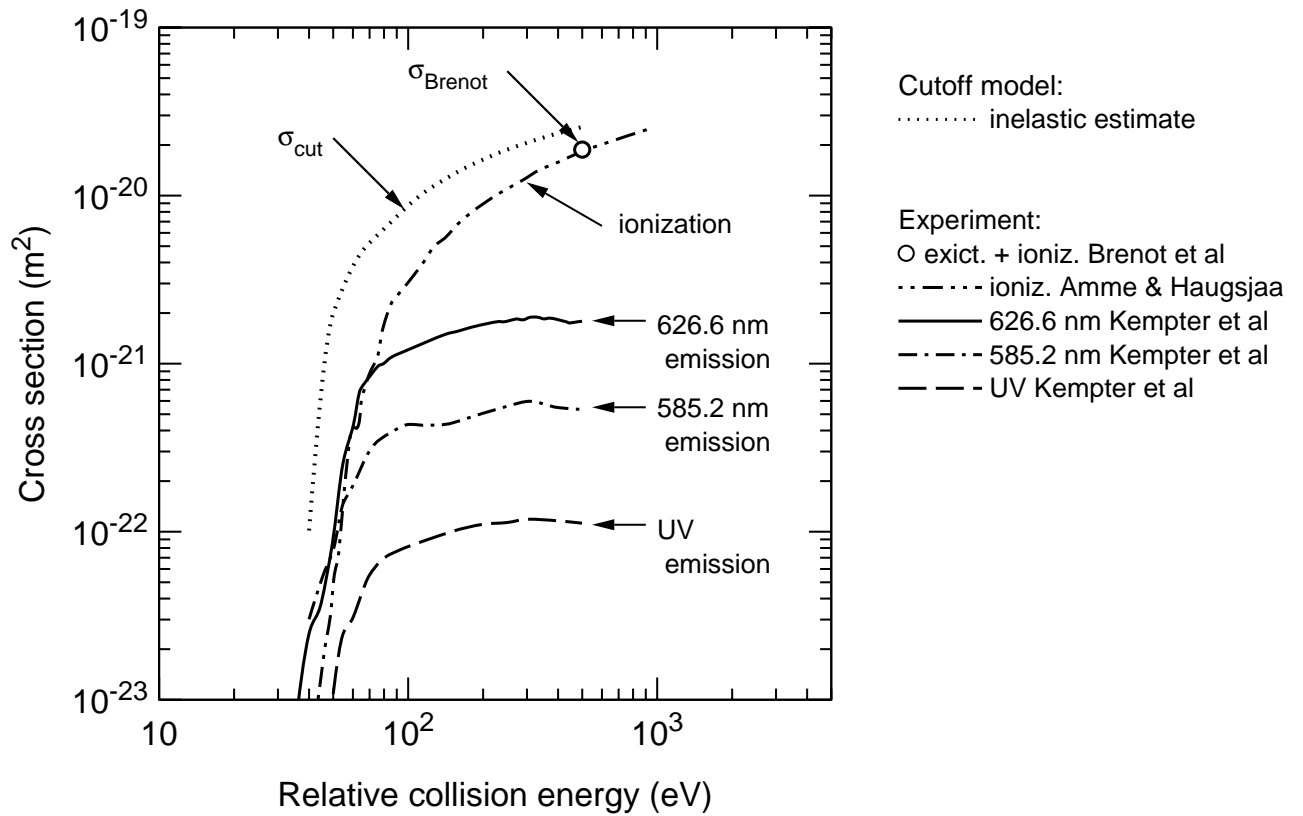


FIG. 9: Excitation and ionization cross sections for symmetric Ne atom-Ne atom collisions. The curves show the results of photon and electron collection experiments integrated over all angles. The points show the results of theoretical calculations and extrapolated scattering experiments integrated over 0 to 90° in center of mass. See text for explanation. The symbols and associated references are:  $\square$  [31];  $\circ$ , [34];  $\triangle, \nabla$ , [35];  $2^1P, 3^1D, 3^3D$  [33, 65]; and  $---$ , [67].

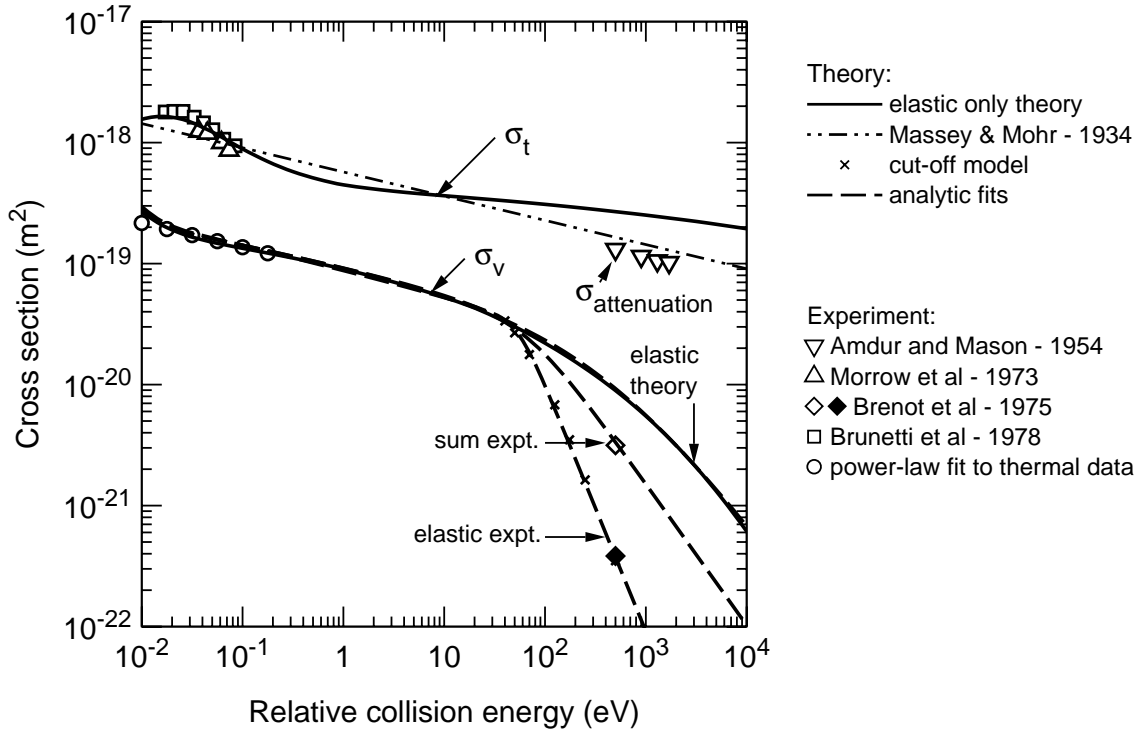


FIG. 10: Total  $\sigma_t$ , viscosity  $\sigma_v$ , and inelastic cross sections for symmetric Ne atom-Ne atom collisions. The solid and short dashed curves show the results of our calculations using the interaction potentials shown by the solid and dashed curves of figure 6. The chain curve is the total cross section from the long-range potential model of Massey and Mohr [72]. The points are viscosity cross sections inferred from viscosity and thermal conductivity measurements, as discussed in the text. The curve marked  $\sigma_t^{vuv}$  and  $\sigma_t^i$  shows the vuv and ionization cross sections [112].

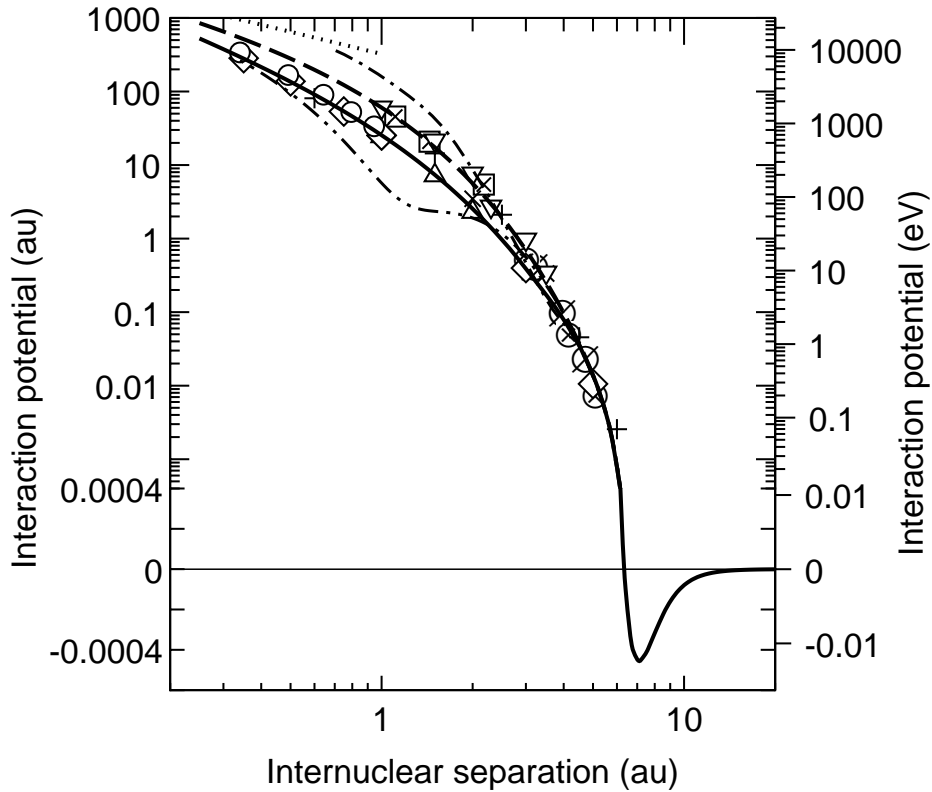


FIG. 11: Interaction potentials versus internuclear separation for Ar atoms with emphasis on the smaller radii. Note that the upper portion of the curves is plotted on a logarithmic scale while the lower portion is plotted on a linear scale. The solid curve shows our adopted interaction potential, while the short-dashed curve shows an alternate potential discussed in the text. The dot-dash line shows the potential used by Robinson [96], while the double-link chain curve shows the recommendation of Aziz and Slaman [97]. Some results of theories are shown by the symbols and references:  $\diamond$ , [47];  $\circ$ , [49];  $+$  [81];  $\nabla$ , [98];  $\triangle$ , [99]; and  $\times$ , [32]. Some potentials based on experiment are shown by the symbols and references:  $\boxtimes$ , [95];  $\otimes$ , [100]; and  $\circ$  [85].

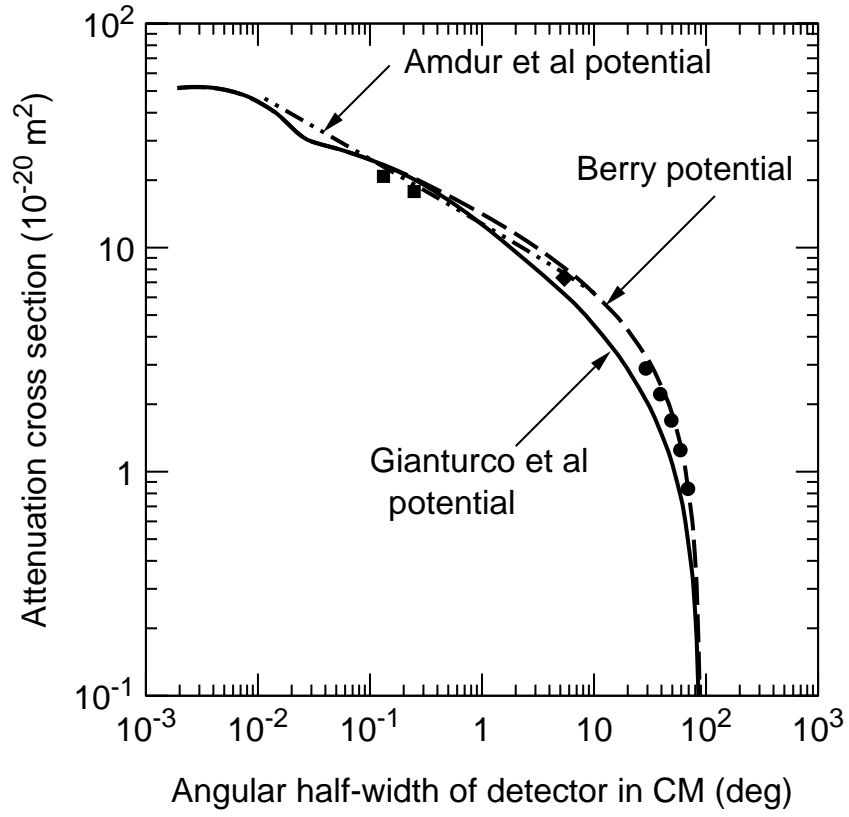


FIG. 12: Attenuation cross sections  $\sigma_{att}$ , for symmetric Ar atom-Ar atom collisions at 500 eV in CM. The solid curves show the results of our calculations of elastic scattering using the interaction potentials shown by the solid curves of figure ???. The dashed and chain curves are the  $\sigma_{att}$  calculated using the Amdur et al[55] and Berry[119] potentials. The symbols and associated references are: + [55];  $\diamond$ , [40]

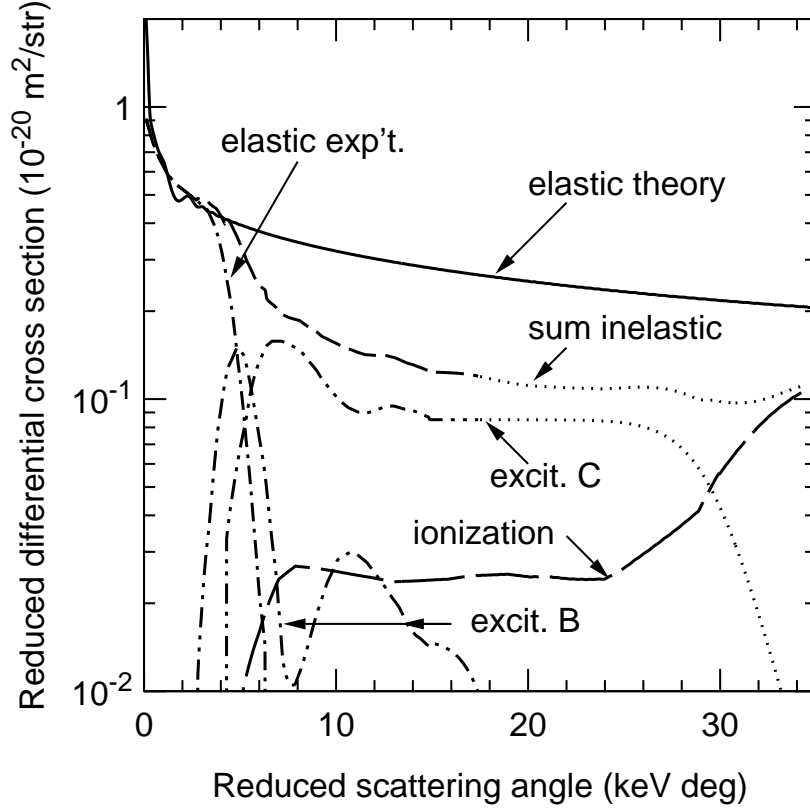


FIG. 13: Elastic and inelastic reduced differential scattering cross sections  $(\theta \sin(\theta) d\sigma(\theta, E)/d\theta)$  versus reduced angle  $(E\theta)$  for a collision energy of 1000 eV. The solid curve is for elastic collisions of  $^{40}\text{Ar}$  with  $^{40}\text{Ar}$  averaged over a Gaussian with a width of  $0.2^\circ$  that removes most of the symmetry oscillations. The elastic experiment curve shows the relative elastic cross sections of Brenot *et al.* [32] normalized to our calculations at small  $\theta$ . The curves marked processes B and C show their normalized excitation data. The ionization cross section is from the relative measurements by Eriksen *et al.* [104] after normalization as discussed in the text. The dotted portions of the curves represent extrapolations of the experiments.

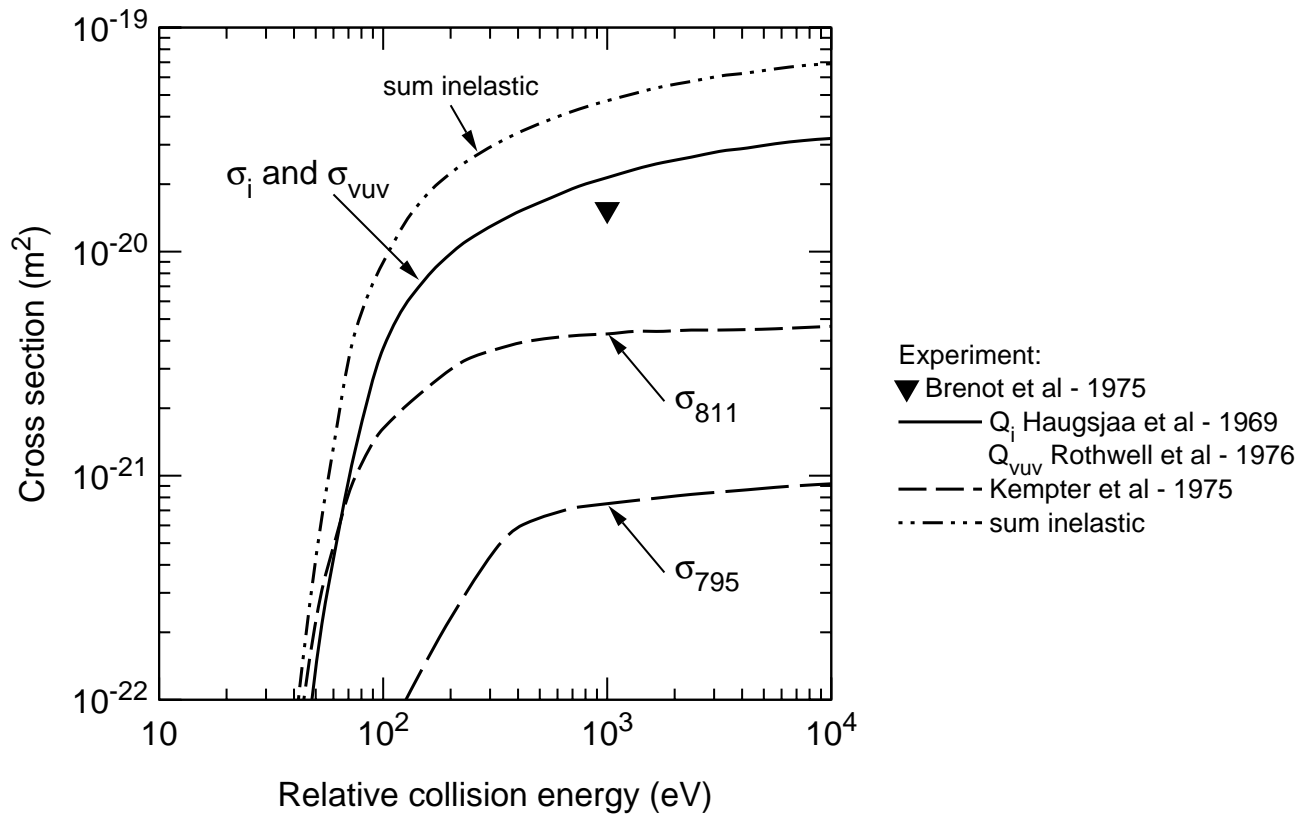


FIG. 14: Excitation and ionization cross sections for symmetric Ar atom-Ar atom collisions. The curves show the results of photon and electron collection experiments integrated over all angles. The point shows the result of scattering experiments integrated over 0 to 90 ° in center of mass. See text for discussion. The curve types and associated references are: — [108, 109]; — — —, [33, 65]; — — —, [33, 65]; and ····, sum inelastic.

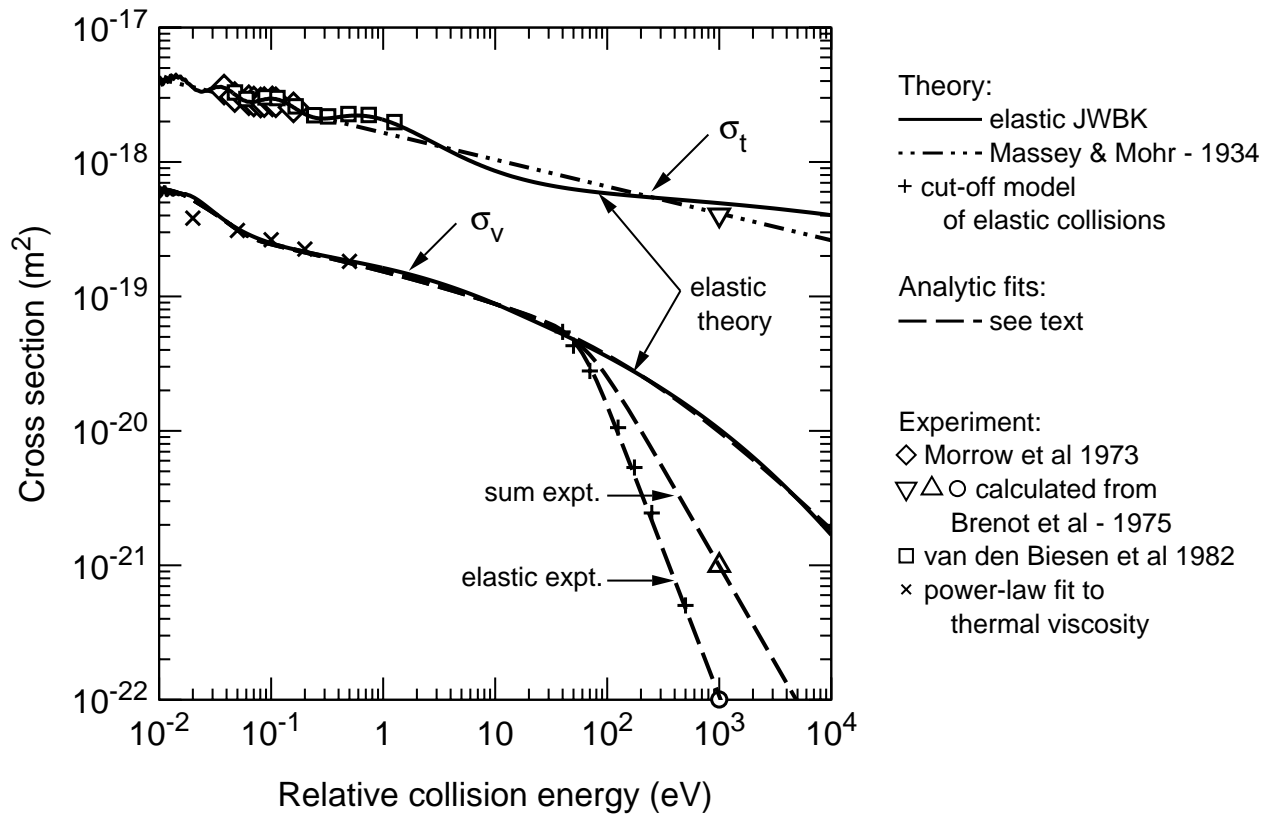


FIG. 15: Total  $\sigma_t$  and viscosity  $\sigma_v$  cross sections for Ar atom - Ar atom collisions. The solid curves show the results of calculations of total and viscosity elastic scattering[94] using the potential from figure 11, while the chain curve is the total cross section calculated considering only the long range potential[72]. The dashed curves are our analytical fits to the model results. The points, their meaning, and their source are: ×, viscosity [94]; ◇, total [31]; ○, elastic viscosity [32]; + cut-off model; ▽, total [32]; △, sum viscosity [32]; and □, total [120].

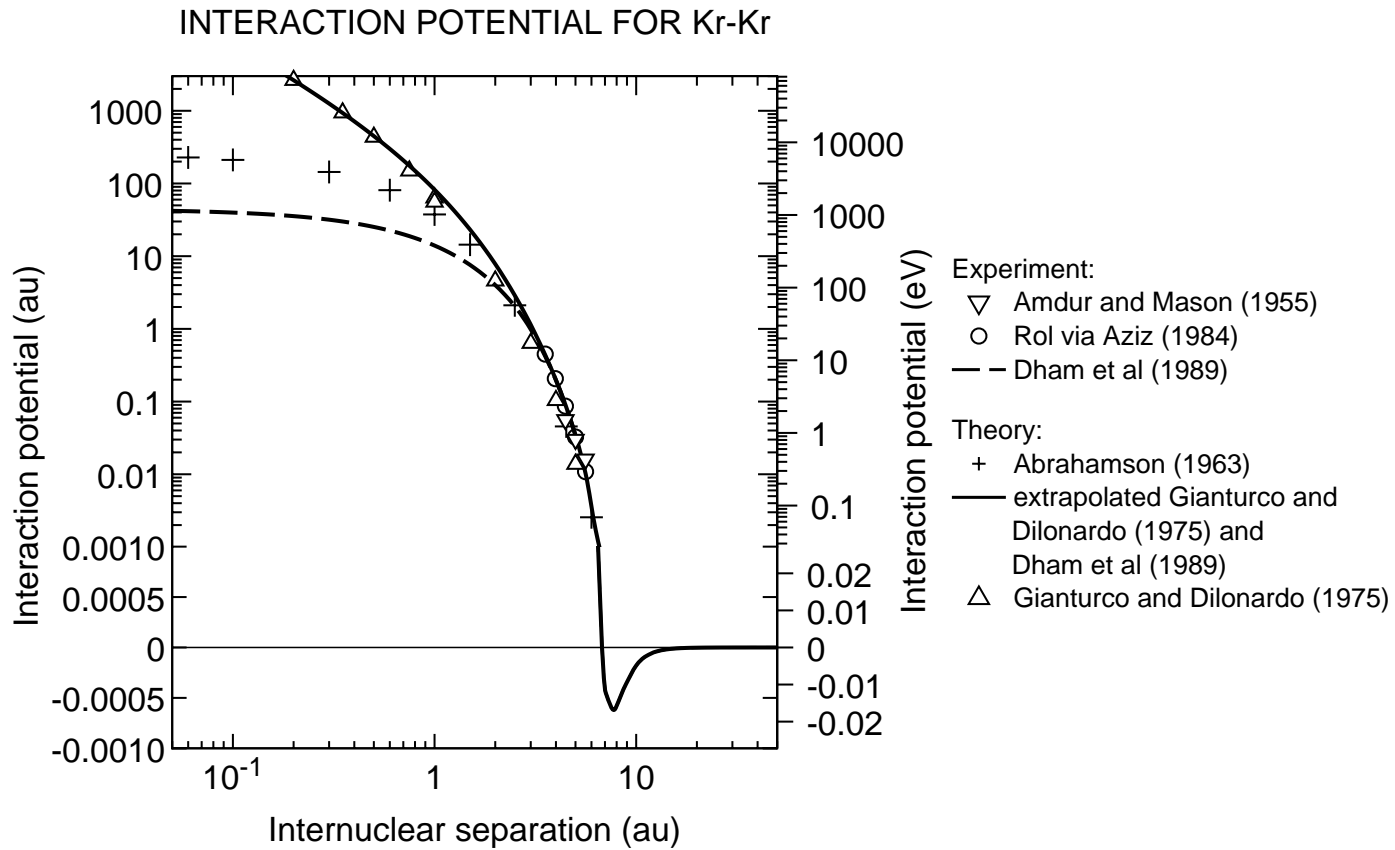


FIG. 16: Interaction potentials versus internuclear separation for Kr atoms with emphasis on the smaller radii. Note that the upper portion of the curves is plotted on a logarithmic scale while the lower portion is plotted on a linear scale. The solid curve shows our adopted interaction potential. The dashed curve shows the recommendation of Dham and Aziz[113]. Some results of theories are shown by the symbols and references: +, [81];  $\triangle$ , [47]. Potentials based on beam experiment are shown by the symbols and references:  $\nabla$ , [82]; and  $\circ$ , [114].

## CROSS SECTIONS FOR Kr-Kr COLLISIONS

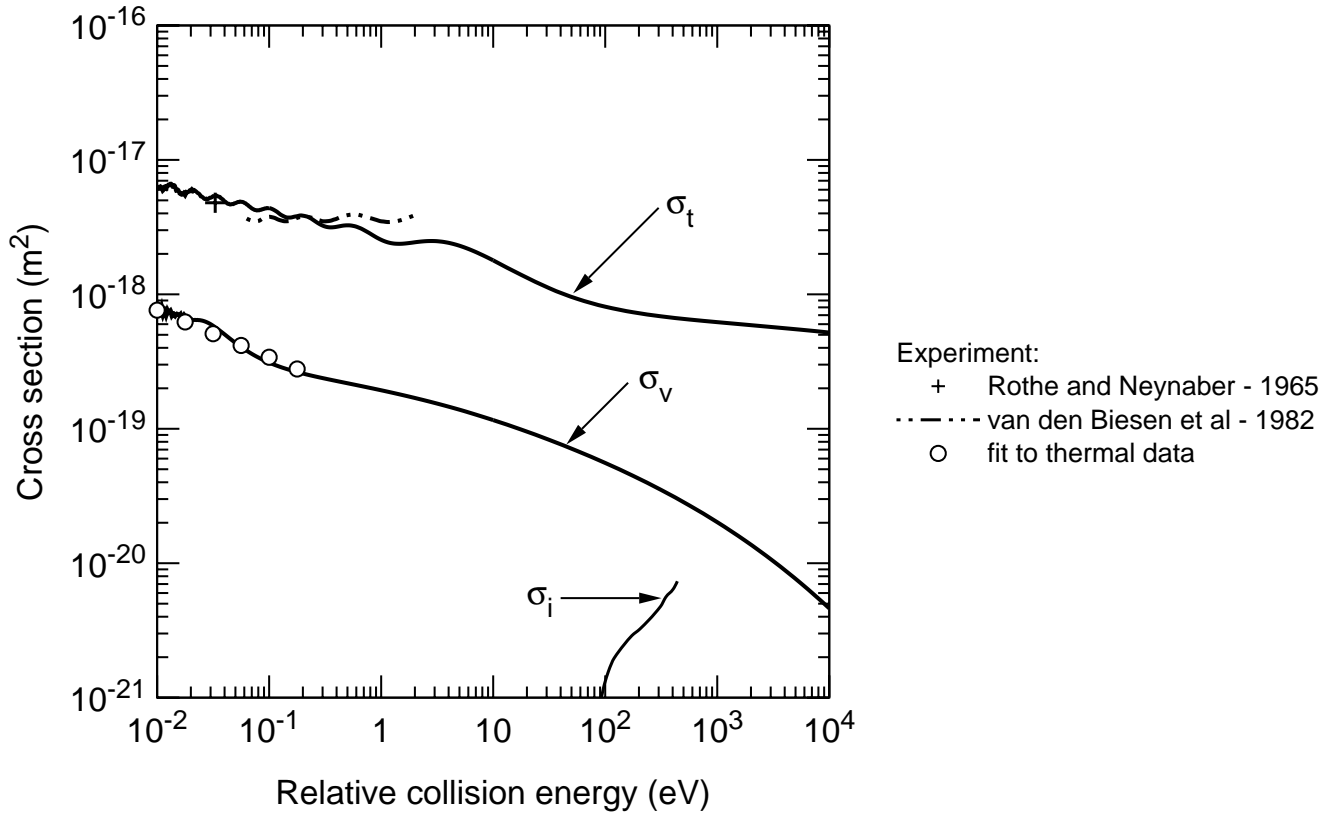


FIG. 17: Total  $\sigma_t$ , viscosity  $\sigma_v$ , and inelastic cross sections for symmetric Kr atom collisions with Kr atoms. The solid curve show the results of our calculations using the interaction potentials shown by the solid and dashed curves of figure 16. The chain curve is the total cross section from the long-range potential model of Massey and Mohr [72]. The circles are viscosity cross sections inferred from a power-law fit to viscosity and thermal conductivity measurements. The curve marked  $\sigma_i^i$  shows the ionization cross section[112].

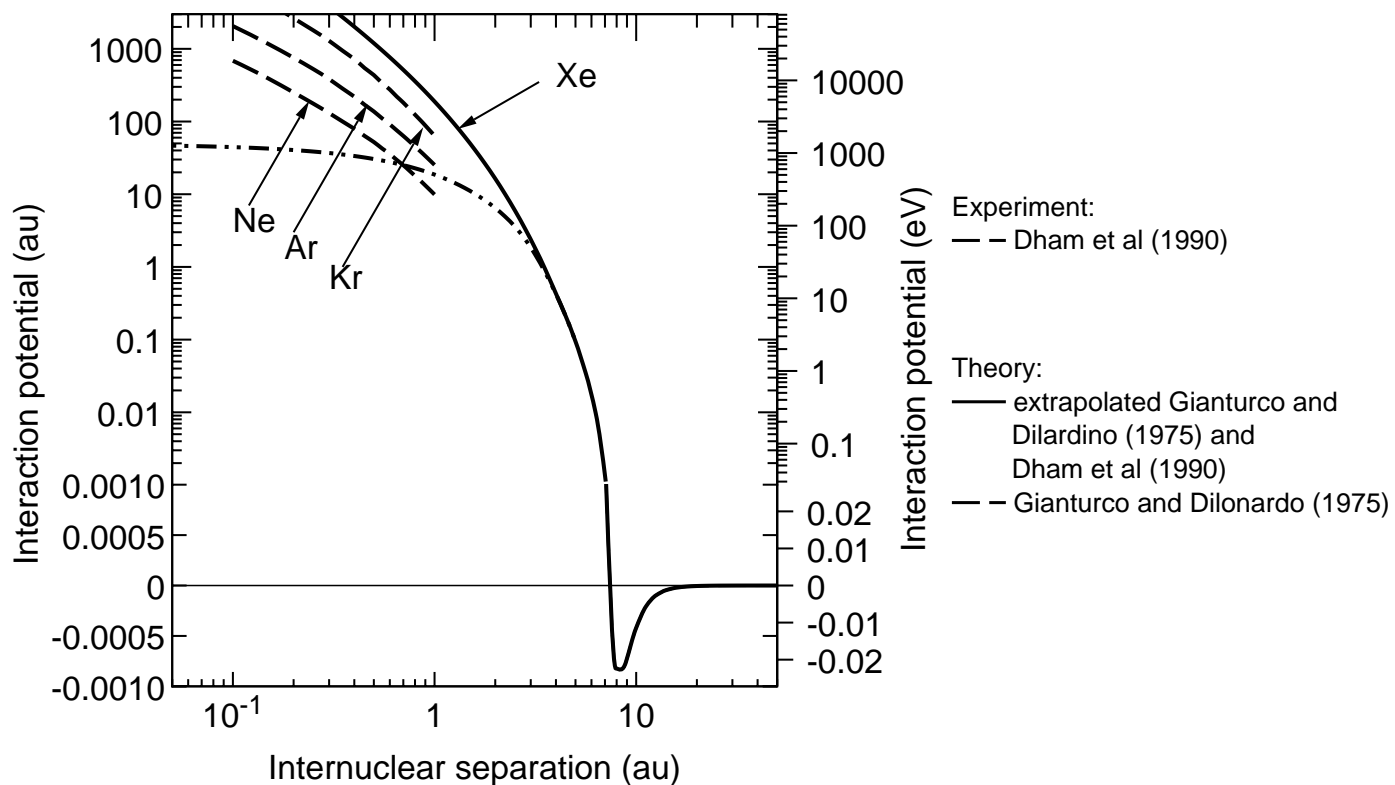


FIG. 18: Interaction potentials versus internuclear separation for Xe atoms with emphasis on the smaller radii. Note that the upper portion of the curves is plotted on a logarithmic scale while the lower portion is plotted on a linear scale. The solid curve shows our adopted interaction potential, while the short-dashed curve shows an alternate potential discussed in the text. The dot-dash line shows the potential used by Robinson [96], while the double-link chain curve shows the recommendation of Aziz and Slaman [97]. Some results of theories are shown by the symbols and references:  $\diamond$ , [47];  $\circ$ , [49]; + [81];  $\nabla$ , [98];  $\triangle$ , [99]; and  $\times$ , [32]. Some potentials based on experiment are shown by the symbols and references:  $\boxtimes$ , [95];  $\otimes$ , [100]; and  $\bigcirc$  [85].

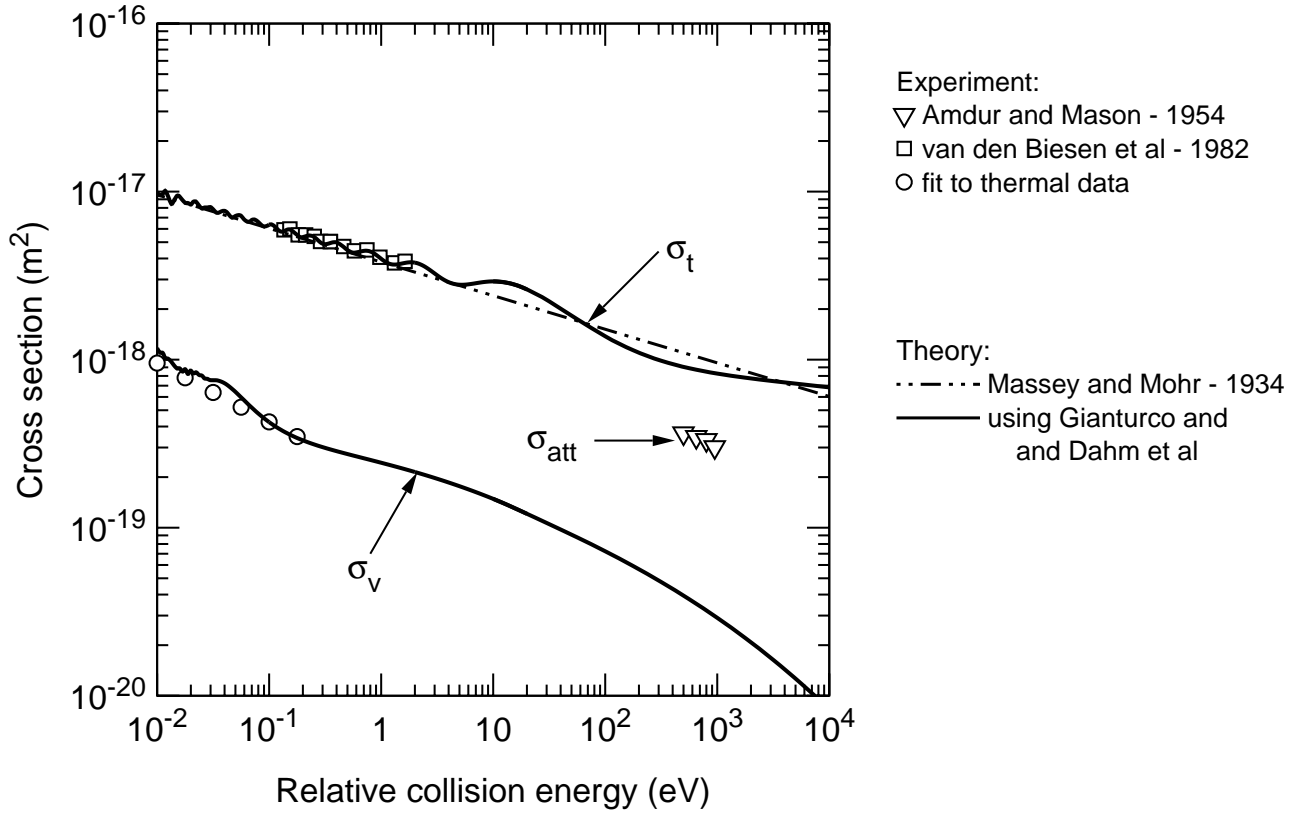


FIG. 19: Total  $\sigma_t$ , viscosity  $\sigma_v$ , and inelastic cross sections for symmetric Xe atom-Xe atom collisions. The solid and short dashed curves show the results of our calculations using the interaction potentials shown by the solid and dashed curves of figure 18. The chain curve is the total cross section from the long-range potential model of Massey and Mohr [72]. The points are viscosity cross sections inferred from viscosity and thermal conductivity measurements, as discussed in the text. The curve marked  $\sigma_t^{vuv}$  and  $\sigma_t^i$  shows the vuv and ionization cross sections [112].

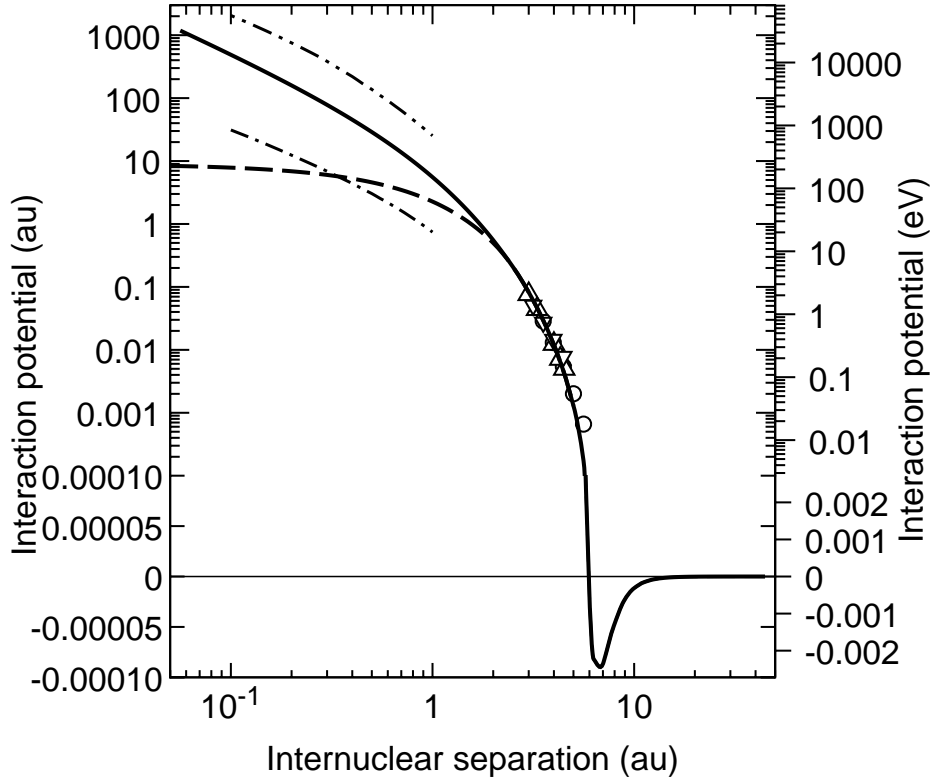


FIG. 20: Interaction potentials versus the internuclear separation of He atoms and Ar atoms with emphasis on the smaller radii. Note that the upper portion of the curves is plotted on a logarithmic scale while the lower portion is plotted on a linear scale. The solid curve shows our adopted interaction potential, while the short-dashed curve shows an alternate potential discussed in the text. The dot-dash line shows the potential used by Robinson [96], while the double-link chain curve shows the recommendation of Aziz and Slaman [97]. Some results of theories are shown by the symbols and references:  $\diamond$ , [47];  $\circ$ , [49];  $+$  [81];  $\nabla$ , [98];  $\triangle$ , [99]; and  $\times$ , [32]. Some potentials based on experiment are shown by the symbols and references:  $\boxtimes$ , [95];  $\otimes$ , [100]; and  $\bigcirc$  [85].

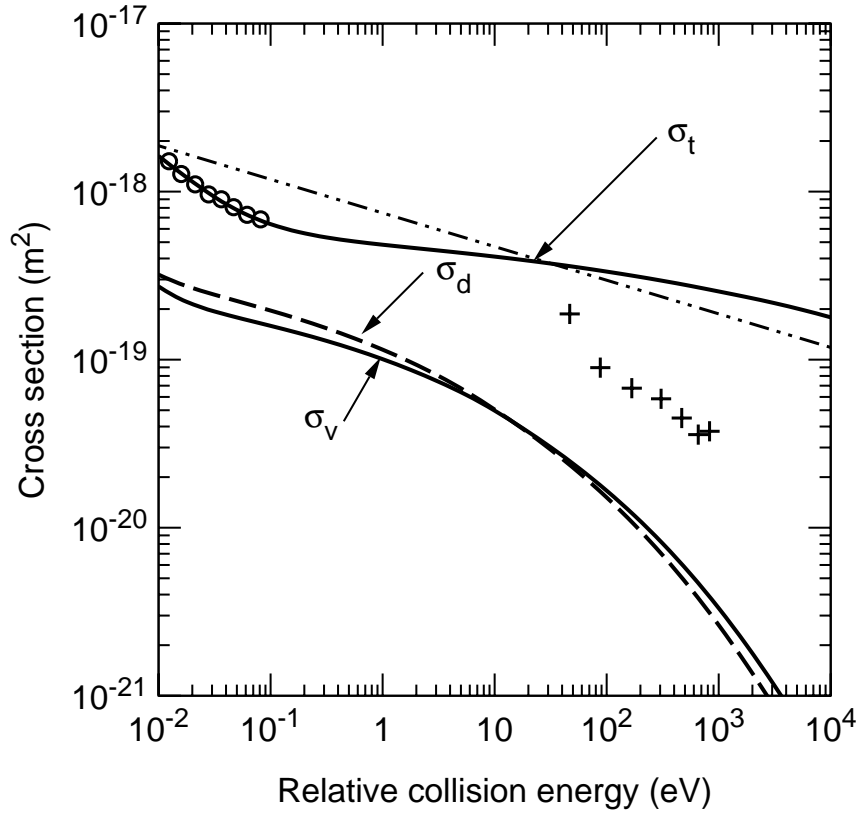


FIG. 21: Total  $\sigma_t$ , viscosity  $\sigma_v$ , and inelastic cross sections for He atom - Ar atom collisions. The solid and short dashed curves show the results of our calculations using the interaction potentials shown by the solid and dashed curves of figure 20. The chain curve is the total cross section from the long-range potential model of Massey and Mohr [72]. The points are viscosity cross sections inferred from viscosity and thermal conductivity measurements, as discussed in the text. The curve marked  $\sigma_t^{vuv}$  and  $\sigma_t^i$  shows the vuv and ionization cross sections [112].

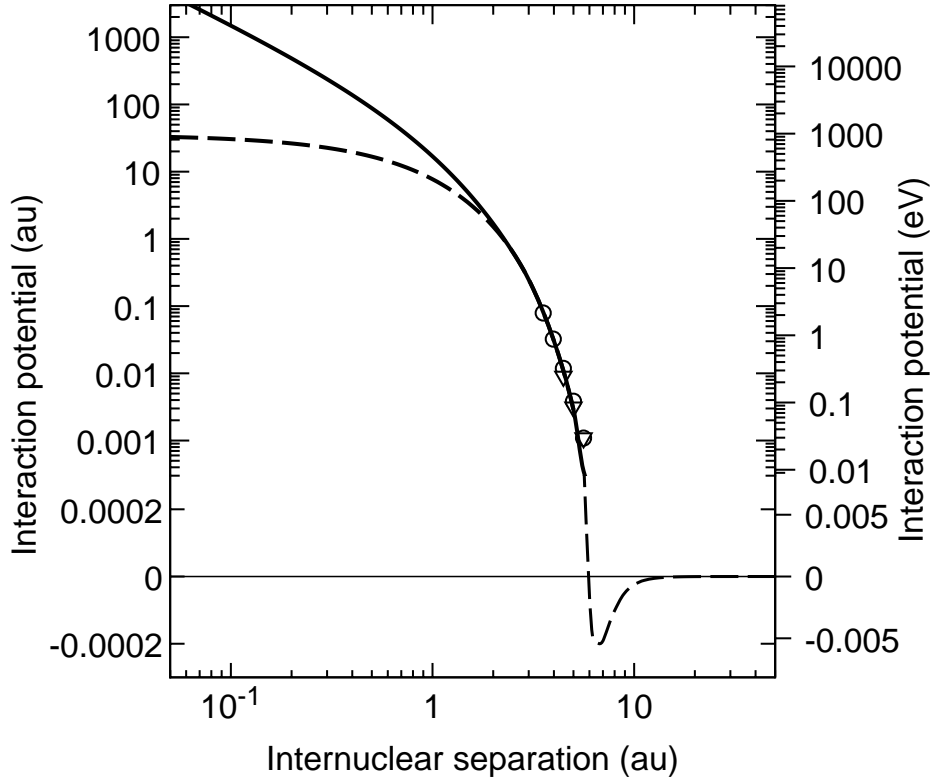


FIG. 22: Interaction potentials versus the internuclear separation of He atoms and Ar atoms with emphasis on the smaller radii. Note that the upper portion of the curves is plotted on a logarithmic scale while the lower portion is plotted on a linear scale. The solid curve shows our adopted interaction potential, while the short-dashed curve shows an alternate potential discussed in the text. The dot-dash line shows the potential used by Robinson [96], while the double-link chain curve shows the recommendation of Aziz and Slaman [97]. Some results of theories are shown by the symbols and references:  $\diamond$ , [47];  $\circ$ , [49];  $+$  [81];  $\nabla$ , [98];  $\triangle$ , [99]; and  $\times$ , [32]. Some potentials based on experiment are shown by the symbols and references:  $\boxtimes$ , [95];  $\otimes$ , [100]; and  $\circ$  [85].

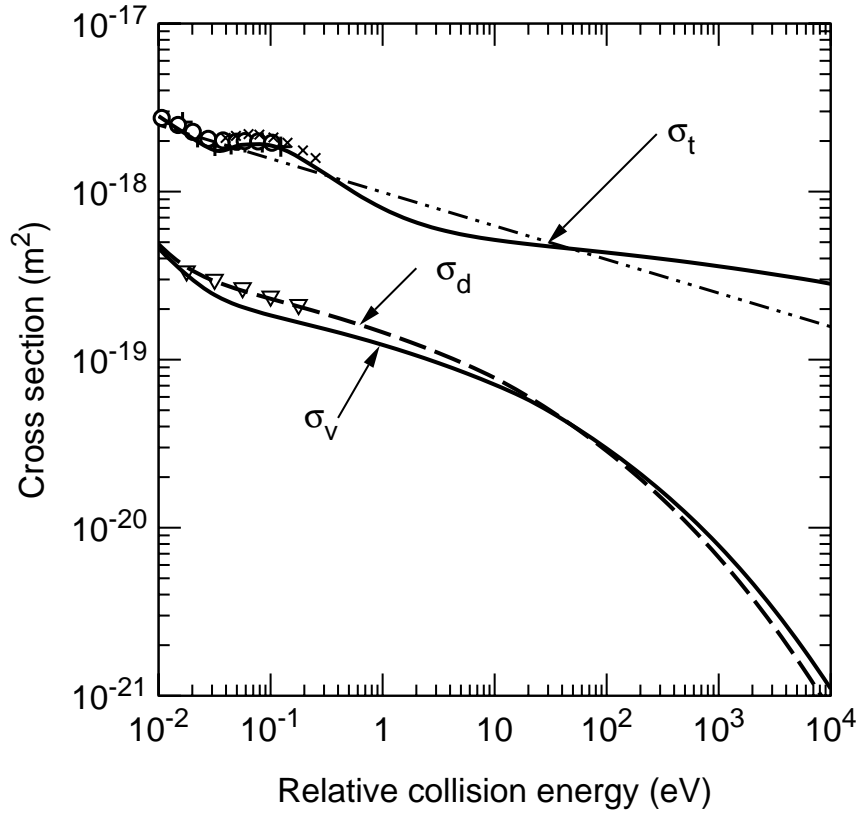


FIG. 23: Total  $\sigma_t$ , viscosity  $\sigma_v$ , and inelastic cross sections for Ne atom-Ar atom collisions. The solid and short dashed curves show the results of our calculations using the interaction potentials shown by the solid and dashed curves of figure 22. The chain curve is the total cross section from the long-range potential model of Massey and Mohr [72]. The points are viscosity cross sections inferred from viscosity and thermal conductivity measurements, as discussed in the text. The curve marked  $\sigma_t^{vuv}$  and  $\sigma_t^i$  shows the vuv and ionization cross sections [112].

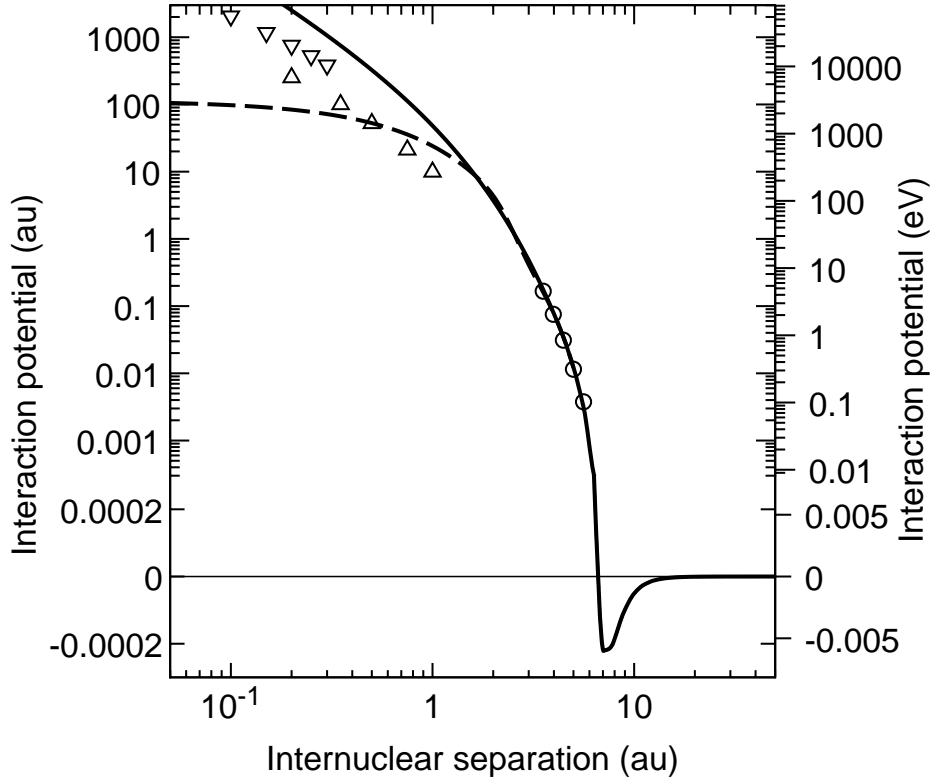


FIG. 24: Interaction potentials versus the internuclear separation for Ne atoms and Xe atoms with emphasis on the smaller radii. Note that the upper portion of the curves is plotted on a logarithmic scale while the lower portion is plotted on a linear scale. The solid curve shows our adopted interaction potential, while the short-dashed curve shows an alternate potential discussed in the text. The dot-dash line shows the potential used by Robinson [96], while the double-link chain curve shows the recommendation of Aziz and Slaman [97]. Some results of theories are shown by the symbols and references:  $\diamond$ , [47];  $\circ$ , [49];  $+$  [81];  $\nabla$ , [98];  $\triangle$ , [99]; and  $\times$ , [32]. Some potentials based on experiment are shown by the symbols and references:  $\boxtimes$ , [95];  $\otimes$ , [100]; and  $\bigcirc$  [85].

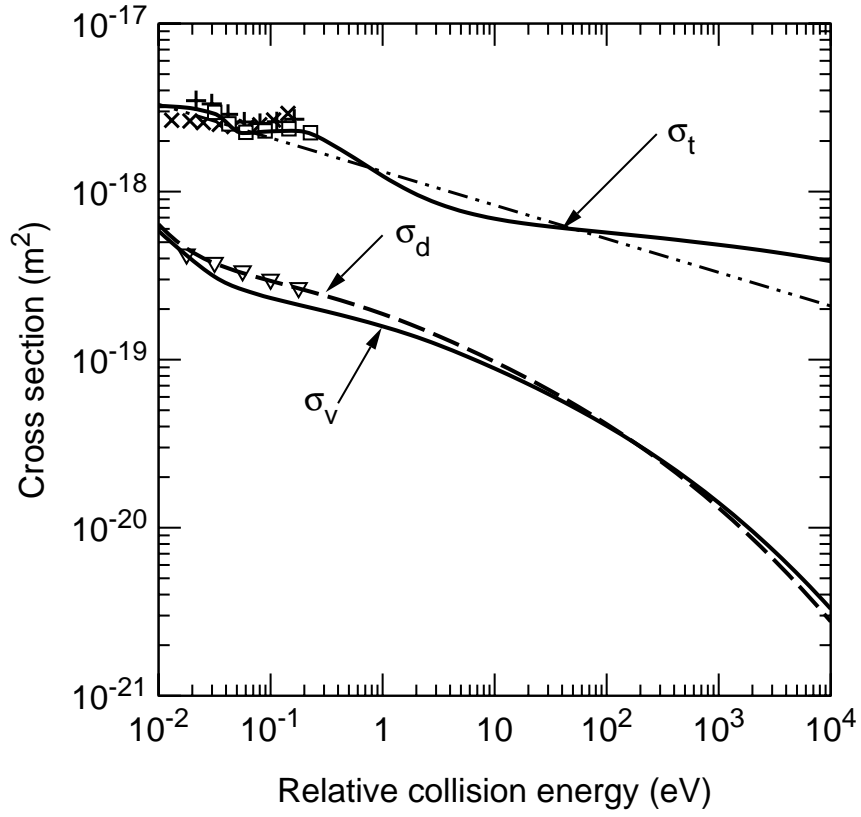


FIG. 25: Total  $\sigma_t$ , viscosity  $\sigma_v$ , and inelastic cross sections for Ne atom-Xe atom collisions. The solid and short dashed curves show the results of our calculations using the interaction potentials shown by the solid and dashed curves of figure 24. The chain curve is the total cross section from the long-range potential model of Massey and Mohr [72]. The points are viscosity cross sections inferred from viscosity and thermal conductivity measurements, as discussed in the text. The curve marked  $\sigma_t^{vuv}$  and  $\sigma_t^i$  shows the vuv and ionization cross sections [112].